ALMA MATER STUDIORUM · UNIVERSITÀ DI BOLOGNA

Scuola di Scienze
Dipartimento di Fisica e Astronomia
Corso di Laurea in Fisica

Large-Eddy Simulation of an Anabatic Wind on an Idealised Geometry

Relatore:
Prof. Federico Porcú

Correlatore:
Dott. Carlo Cintolesi

Presentata da:
Stefano Franzoni

Anno Accademico 2019/2020

Abstract

La presente tesi propone una simulazione numerica Large-Eddy Simulation (LES) con Near-Wall Resolution (NWR) in OpenFOAM di un flusso anabatico all'interno di una geometria semplificata. Il caso proposto consiste nella riproduzione del flusso che si instaura al di sopra di un piano inclinato di 30°, liscio e infinitamente esteso, avendo imposto una buoyancy costante sulla superficie, il numero di Grashof $Gr = 2.1 \times 10^{11}$ e il numero di Prandtl $Pr = 1$. La prima parte del lavoro offre una panoramica dei principali aspetti caratterizzanti la fluidodinamica computazionale e utili a fornire un contesto teorico per il caso presentato. In particolare, si descrivono i fondamenti del metodo di discretizzazione ai volumi finiti impiegato in OpenFOAM. Con l'intento di mostrare le principali motivazioni che giustificano l'introduzione dell'approccio LES, si forniscono le basi della teoria della turbolenza di Kolmogorov. La discussione del metodo LES viene conclusa con la presentazione del modello di Smagorinsky, impiegato nella simulazione. La seconda parte si focalizza sull'esposizione del caso simulato. Una volta introdotte le equazioni che governano il sistema, si forniscono i dettagli delle impostazioni della simulazione, esponendo le modifiche apportate al solutore. Attraverso i grafici prodotti, la simulazione viene validata tramite il confronto con i risultati dalla Direct Numerical Simulation (DNS) effettuata da Giometto et al. [MG17]. Contestualmente, si offre una discussione dei risultati dal punto di vista fisico, individuando le principali proprietà delle componenti medie e della turbolenza, nonchè mostrando le strutture che caratterizzano istantaneamente il moto.

Abstract

This bachelor thesis proposes a Large-Eddy Simulation (LES) with Near-Wall Resolution (NWR) of an anabatic flow using a simplified geometry. The case is simulated in Open-FOAM and it reproduces the flow developing over a smooth, infinite, 30° inclined plane, having imposed a constant buoyancy on the surface, the Grashof number $Gr = 2.1 \times 10^{11}$ and the Prandtl number $Pr = 1$. The first part of this work offers an overview on the main features of the computational fluid dynamics, so as to provide a theoretical context for the presented case. In particular, the Finite Volume Method (FVM) employed in OpenFOAM is described in its fundamental aspects. With the purpose to motivate the introduction of the LES approach, the bases of the Kolmogorov's theory on turbulence are presented. The Smagorinsky model adopted in the simulation, concludes the discussion on the LES method. The second part focuses on the description of the simulated case. Having introduced the set of the governing equations, the simulation settings are provided, and the modifications brought to the solver are described. The simulation is validated by comparing the results with the Direct Numerical Simulation (DNS) performed by Giometto et al.[MG17]. At the same time, the data are analysed from a physics perspective, so as to point out the most relevant mean flow and turbulence features, as well as instantaneous flow characteristics.

Contents

Introduction

Complex and inclined terrains are quite likely to produce the phenomenon of anabatic and katabatic winds. Both these phenomena are induced by the differential heating of the ground and the surrounding atmosphere, caused by the Sun on a daily basis. Their names come from the Greek terms $\alpha\nu\acute{\alpha}\beta\alpha\sigma\iota\varsigma$ and $\kappa\alpha\tau\acute{\alpha}\beta\alpha\sigma\iota\varsigma$, meaning respectively upwards and downwards: they are also known as up-slope and down-slope winds.

Anabatic winds are generated when the solar radiation heats up the ground surface, generating convective motions in the adjacent boundary layer. Depending on the slope angle, the wind generated tends to follow the ground surface, showing occasional plumes upwards, towards the outer layers. In some cases, along with this upward flow, colder and denser air is pulled downwards following an outer path, typically approaching the ground surface at the starting point of the slope. Since up-slope winds occur daily, a fully developed Convective Boundary Layer (CBL) characterizes the atmospheric background, making their study more challenging [CR05].

Katabatic winds, on the other side, usually occur in the shadowed sides of the mountains or at night. A less intense or absent solar radiation characterizes these slopes, causing the air within the boundary layer to be colder than that in the outer profile at the same height. As a result, this layer tends to sink downwards, while warmer air takes its place at the top of the slope. When occurring at night-time, unlike anabatic winds, down-slope flows develop within a stable boundary layer [CR05].

The interaction between the ground and the adjacent boundary layer is at the heart of these phenomena and turbulence plays a fundamental role in the complex thermodynamic processes arising.

Considering the anabatic flows, recently, many studies have been conducted so as to understand their properties. One of the most relevant field of research is that concerning the diffusion and transport of air pollutants, whose prediction is particularly important in areas with complex terrains [TK89]. The effect of the interaction between the air pollutants and these mountain flows is connected with the characteristics of the underlying CBL, which are highly dependent on the circulations on a synoptic scale. The problem has been faced both experimentally and numerically, in the latter case trying to reproduce increasingly complex situations.

Considering the numerical simulations, a few Direct Numerical Simulations (DNS)

and Large-Eddy Simulations (LESs) have been performed. Let us briefly introduce the ones relevant for the present simulation. Following the one-dimensional, laminar slope flow described by Prandtl [Pra42], Schumann [Sch90] was one of the first to tackle the problem fully considering three-dimensional features and turbulent effects. Towards the end of the 80s, he performed a LES of an infinite planar slope surrounded by a stratified atmosphere, by imposing a fixed heat flux through the rough surface. In 2009, Fedorovich and Shapiro [EF09] conducted a DNS simulation of an infinite, thermally perturbed, planar slope. In this case, a homogenous surface buoyancy flux was imposed. In 2017, Giometto et al. [MG17] carried out a DNS simulation of both anabatic and katabatic flows over an inclined, smooth, infinite planar slope at high Grashof numbers.

In the present thesis, one of the cases reported by Giometto et al [MG17]. has been reproduced by means of a LES. This numerical approach resolves the large scales of motion and models only the small sub-grid scales, that are less energetic and more universal (hence, they can be more effectively modelled). The LES allows to reproduce a complex thermodynamic system using a fraction of the number of the computational grid required by DNS: in the present case, the computational mesh have been 1/64 smaller than the equivalent DNS mesh. Nonetheless, all the transient flow features of the flow are reproduced with satisfactory accuracy.

In the first part, an overview on the basic concepts of computational fluid dynamics is offered, so as to provide a theoretical background for the presented case. The LES approach is introduced, outlining the fundamental premises involved. In the second part, the simulated case is presented, the results are discussed and compared with the DNS reported by Giometto et al. [MG17]. The data are analysed from a physics perspective to point out the characteristic phenomena underlying the idealised anabatic flow under study.

Chapter 1

Numerical methods

In computational fluid dynamics, mathematical models are numerically solved to study in details specific physical systems. The basic equations governing a fluid modelled as a continuum are the mass, the momentum and the energy conservation equations. These three equations are coupled together with a certain amount of closure constraints, whose choice is made according with the physical model adopted to describe the system. For example, let us consider a physical system similar to that considered for the present simulation. Taking into account a Newtonian and incompressible fluid in the Boussinesq approximation with kinematic viscosity ν and thermal diffusivity κ, then the set of governing equations reads as follows [PK04]:

$$
\begin{aligned}
\frac{\partial u_j}{\partial x_j} &= 0 \\
\frac{Du_i}{Dt} &= -\frac{\partial \Pi}{\partial x_i} + \frac{\rho - \rho_0}{\rho_0} g_i + \frac{\partial}{\partial x_j}\left[\nu \frac{\partial u_i}{\partial x_j}\right] \\
\frac{DT}{Dt} &= \frac{\partial}{\partial x_j}\left[\kappa \frac{\partial T}{\partial x_j}\right] \\
\rho &= \rho_0 \left[1 - \alpha \left(T - T_0\right)\right]
\end{aligned}
\tag{1.1}
$$

where ρ is the fluid density, α its thermal expansion coefficient, T the temperature, Π is the deviation of the kinematic pressure from the hydrostatic background and $\rho_0 = \rho(T_0)$, being T_0 a costant reference temperature. Also, in this last set of equations, D/Dt is the material derivative, defined as follows:

$$
\frac{D}{Dt} = \frac{\partial}{\partial t} + u_j \frac{\partial}{\partial x_j}
\tag{1.2}
$$

In Eq.1.1, the first equation represents the mass conservation for an incompressible fluid, the second the momentum conservation, the third the energy conservation and the fourth is part of the Boussinesq approximation (such approximation will be explained in the

next chapter). It is worth underlining that the material derivative in the momentum equation entails the presence of a non-linear velocity term, namely the advective term. Hence, the set in Eq.1.1 is a system of coupled, non-linear partial differential equations.

In order to numerically solve the system of equations in Eq.1.1, a discretization of both space and time needs to be specified. The calculation of the relevant field is performed at a discrete number of spatial points, which form the computational grid.

In general, according to the graph theory, meshes are classified in two main categories, namely, structured and unstructured meshes. The first ones are characterized by a grid of cells whose connectivity is regular, i.e. internal cells are connected with a fixed number of adjacent cells. This feature entails that a mesh of this type can be made up by either hexahedra (in a three-dimensional space) or quadrilateral (in two dimensions), and its data can be stored in lists. On the other hand, unstructured meshes show irregular connectivity, providing more flexibility when dealing with complex geometries, at the cost of a greater computer memory consumption and worse performances [FM16].

Usually, space discretization is provided before the simulation is started, and it remains the same throughout the temporal iterations. In some cases, however, it may be useful or necessary to define dynamic meshes, whose geometrical properties may be changed according to relevant parameters of the simulation [Jas09]. Similarly, temporal discretization may be defined as a constant step, or may vary, as well. In this case, a typical parameter used to adjust the time step is the Courant number, which will be defined in the next section.

Given a space-time discretization, the system of partial differential equations is converted into a linear system. This procedure can be obtained through different methods, the most common ones being the finite volumes, finite differences and finite elements methods. In the following section, the finite volumes method is briefly described. This is the method employed in the OpenFOAM code and it will be exposed using the assumptions actually imposed on the present simulation.

1.1 Finite volumes method

To introduce the Finite Volumes discretization Method (FVM), it may be useful to recall the prototype of the conservation equation for a scalar ϕ:

$$\frac{\partial (\rho \phi)}{\partial t} + \frac{\partial (\rho u_j \phi)}{\partial x_j} = \frac{\partial}{\partial x_j} \left[\Gamma_\phi \frac{\partial \phi}{\partial x_j} \right] + Q_\phi \qquad (1.3)$$

where ρ is the fluid density, Γ_ϕ is the diffusion coefficient of the scalar ϕ and Q_ϕ represents a source term. For the sake of clarity, let us underline that Einstein's convention of summation over repeated indexes is hereafter adopted. Considering Eq.(1.3), the first term on the left hand side represents the transient term, while the second one is the

convection term. On the right hand side, the first one is the diffusion term and the second one a source term.

The purpose of any discretization procedure is to replace a differential equation in the continuum with a set of algebraic equations. In the finite volumes approach, the first step is to integrate over a time step Δt and over a computational cell volume V_C and then to use the divergence theorem to transform volume integrations into surface integrations [FM16]. In the following, a static, structured and orthogonal mesh is assumed, while, the time step is maintained constant[1]. Under these assumptions, the first steps can be summarised as follows:

$$\int_{\Delta t} \int_{V_C} \frac{\partial (\rho \phi)}{\partial t} dV \, dt + \int_{\Delta t} \int_{V_C} \frac{\partial (\rho u_j \phi)}{\partial x_j} dV \, dt =$$
$$= \int_{\Delta t} \int_{V_C} \frac{\partial}{\partial x_j} \left[\Gamma_\phi \frac{\partial \phi}{\partial x_j} \right] dV \, dt + \int_{\Delta t} \int_{V_C} Q_\phi dV \, dt$$

$$\int_{\Delta t} \int_{V_C} \frac{\partial (\rho \phi)}{\partial t} dV \, dt + \int_{\Delta t} \oint_{\partial V_C} \rho u_j \phi dS_j \, dt =$$
$$\int_{\Delta t} \oint_{\partial V_C} \Gamma_\phi \frac{\partial \phi}{\partial x_j} dS_j \, dt + \int_{\Delta t} \int_{V_C} Q_\phi dV \, dt \qquad (1.4)$$

Now, let us first consider the transient term. Assuming sufficiently smooth solutions, this term reads as follows:

$$\int_{\Delta t} \int_{V_C} \frac{\partial (\rho \phi)}{\partial t} dV \, dt = \int_{\Delta t} \frac{\partial}{\partial t} \left[\int_{V_C} \rho \phi dV \right] dt \cong \int_{\Delta t} \frac{\partial (\rho \phi)_C}{\partial t} V_C dt \qquad (1.5)$$

In the last equivalence in Eq.(1.5), $(\rho \phi)_C$ specifies that $\rho \phi$ is evaluated at the cell centroid, thus leading to a first order approximation. Such approximation is often referred to as the midpoint rule [FM16], and it must be underlined that more complex and accurate interpolation are available. Now, let us consider the flux integrals. It may be useful to group these terms and to introduce the following notation:

$$J_i = \rho u_i \phi - \Gamma_\phi \frac{\partial \phi}{\partial x_i} \qquad (1.6)$$

Since each cell surface is composed by six faces, the surface flux integral can be decomposed into the sum of the integrals over each single cell face. As a consequence, dS_i is constant over a single face. Therefore, considering a second-order Gaussian quadrature

---

[1]This last assumption differs from the settings of the present simulation and it is assumed for the sake of brevity.

integration, each term of the sum can be obtained by evaluating J_i at the face centroid, leading to:

$$\int_{\Delta t} \oint_{\partial V_C} J_j dS_j dt = \int_{\Delta t} \sum_{f_i} \oint_{f_i} J_j dS_j dt \cong$$

$$\cong \int_{\Delta t} \sum_{f_i} (J_j)_{f_i} S_j^{(f_i)} dt \qquad (1.7)$$

where, $(J_j)_{f_i}$ indicates that J_j is evaluated at the face centroid. Taking into account the source term, it is possible to apply the midpoint rule, and the production term reads as follows:

$$\int_{\Delta t} \int_{V_C} Q_\phi dV dt \cong \int_{\Delta t} (Q_\phi)_C V_C dt \qquad (1.8)$$

If the production term contains a gradient (for example, the pressure gradient in the Navier-Stokes Equation), it can be linearized using the Gauss theorem. In what follows, Q_ϕ will be treated like in Eq.(1.8). By substituting Eq.(1.5), Eq.(1.7) and Eq.(1.8) into Eq.(1.4), one gets the following equation:

$$\int_{\Delta t} \frac{\partial (\rho\phi)_C}{\partial t} V_C dt + \int_{\Delta t} \sum_{f_i} (J_j)_{f_i} S_j^{(f_i)} dt = \int_{\Delta t} (Q_\phi)_C V_C dt \qquad (1.9)$$

Now, let us consider time integrals. So far, only Δt has been shown to indicate the extent in time of such integration. Indeed, in terms of its limits, the integral is to be computed over the range $[t - \Delta t/2, t + \Delta t/2]$. Any term in Eq.(1.9) but the transient one, is integrated using the midpoint rule: again, this is a second order approximation. On the other side, the transient term can be explicitly evaluated, though a scheme needs to be provided to express the fields in $t + \Delta t/2$ and $t - \Delta t/2$ as a function of their values at some instant $t + n\Delta t$ (here, n is an integer). The most suitable scheme can be chosen among the ones defined in the finite differences methods. For example, here the Second Order Upwind Euler Scheme[2] (SOUE) is considered [FM16]:

$$\begin{aligned} (\rho\phi)_C^{t+\Delta t/2} &= \frac{3}{2} (\rho\phi)_C^t - \frac{1}{2} (\rho\phi)_C^{t-\Delta t} \\ (\rho\phi)_C^{t-\Delta t/2} &= \frac{3}{2} (\rho\phi)_C^{t-\Delta t} - \frac{1}{2} (\rho\phi)_C^{t-2\Delta t} \end{aligned} \qquad (1.10)$$

Similarly, a finite difference scheme is to be specified to compute the diffusion component in the flux (see Eq.(1.6)) and to interpolate the data to face centroids. For example, the diffusion component may be evaluated using a linear interpolation between adjacent cells, while interpolation may be done via central or upwind differencing [Gre15].

---

[2]This is the actual time scheme employed in the present simulation.

As a result, any term in Eq.(1.9) except the transient one can be linearized and it can be expressed as a function $L\left(\phi_{C_i}^t\right)$ of $\phi_{C_i}^t$, where i ranges over the present cell and the adjacent ones. By substituting these last observations and Eq.(1.10) into Eq.(1.9), one gets to the following result:

$$\frac{3\left(\rho\phi\right)_C^t - 4\left(\rho\phi\right)_C^{t-\Delta t} + \left(\rho\phi\right)_C^{t-2\Delta t}}{2\Delta t}V_C + L\left(\phi_{C_i}^t\right) = 0 \tag{1.11}$$

The result in Eq.(1.11) represents the sought-after set of algebraic equations and it can be solved iteratively in time.

Boundary conditions must specified, and this requires to impose constraints on all bounding surfaces. In addition, for transient problems, initial conditions are to be set for all the internal fields.

The Courant–Friedrichs–Lewy Condition

As far as convergence is concerned, the previous approximation methods require the Courant–Friedrichs–Lewy (CFL) condition to be satisfied. For a three-dimensional problem, the condition can be defined as follows [Ope]:

$$Co \equiv \frac{\Delta t}{2V_C} \sum_{f_i} \left|(u_j)_{f_i} S_j^{(f_i)}\right|$$
$$Co \leq C_{max} \tag{1.12}$$

where $(u_j)_{f_i}$ is the velocity interpolated on the cell face f_i and $S_j^{(f_i)}$ is the face normal surface vector. C_{max} can be set equal to 1, even though lower C_{max} values are recommended (for example, $C_{max} = 0.5$). As anticipated in the previous section, Co is often employed to adjust Δt so that the CFL requirement is met.

The most relevant implications of the results exposed in this section can be outlined as follows:

1. The CFL condition is a useful tool to adjust the time step during a simulation, contributing to its efficiency and economy.

2. FVM is intrinsically conservative. Indeed, any flux leaving the computational cell is seen as an opposite, in-going flux from the adjacent cell.

3. FVM requires averaging the field values over a computational cell. This entails a loss of information about any field property whose characteristic space length is smaller than the grid size. In case of nonlinear equations (such as the momentum equation in fluid dynamics, see Eq.1.1), any scale length interacts with each other, each of them contributing to produce the total field solution. As a consequence, the grid size plays a fundamental role in the accuracy of the solution, and a certain knowledge of the specific phenomenon is crucial to set it correctly.

CFD simulations might need very refined meshes, thus having a very high computational cost. Therefore, two options are offered, which are relevant for the present simulation: first, to enhance the computing power in order to resolve every scale of motion in any setup, second, to introduce models for the sub-grid scales of motion, so that coarser meshes may be used without losing in accuracy. The first approach leads to the Direct Numerical Simulations (DNSs), while the second one characterizes the Large-Eddy Simulations (LESs). It must underlined that a third main approach exists, which will not be taken into account here, namely that of Reynolds Averaged Navier-Stokes (RANS). In what follows, the LES approach will be discussed.

1.2 Turbulent flows: an overview

Turbulence is a kinematic condition in which a flow exhibits random-like variations of its kinematic quantities and it is characterized by three-dimensional vorticity. A comprehensive, quantitative description of this phenomenon is still to be found and even its definition is challenging. For the sake of brevity, the main features shared by turbulent flows can be outlined as follows [PK04]:

1. Randomness can be considered as the basic qualitative first impression of turbulence. At the same time, this stochastic behavior seems to produce certain distinguishable patterns, even showing approximate self-similar shapes. Swirls, vortexes, plumes and jets are just a few examples of these structures.

2. Non-linearity is probably at the heart of turbulence. In certain conditions, small perturbations in the flow may be enhanced and cause a cascade of collateral phenomena and structures, eventually leading to the turbulent regime. If this happens, all the main variables vary in an apparently unpredictable way.

3. Three-dimensional vorticity is a key feature in turbulent flows. In fact, an extremely rich spectrum of vortex sizes characterizes these flows, going from those as wide as the entire domain, to those whose typical length is of the order of the Kolmogorov scale (see Eq.(1.17)). Most of the energy is contained in larger vortexes, and three-dimensional stretching makes them collapse into smaller ones. This process leads to a cascade, bringing energy from the largest down to the smallest scales. At this stage, the extremely intense curl of these structures is associated with significant spatial variations in the velocity field, leading to high viscous dissipation rates. As a result, all turbulent phenomena exhibit an increase in momentum and heat transfer, as well as in friction and drag.

To summarize these points, turbulence is a stochastic fluid state, in which non-linearity and three-dimensional vorticity cause an increase in diffusivity and viscous dissipation. As a consequence of its random behavior, a statistical analysis is useful to extract the

average features of a turbulent flow. Hence, both first and second order statistics are usually computed: the main ones are mean values, standard deviations, covariances and auto-correlations. In addition, spectral analysis may be performed, in order to understand how energy is distributed over the whole length scale range.

The Kolmogorov's Theory of Turbulence

In 1940s, Kolmogorov developed his theory on turbulent energy spectra. Without going into much detail, the basic concepts of the theory advanced by Kolmogorov are discussed. First of all, let us introduce the so-called Reynolds velocity decomposition:

$$u_i = \langle u_i \rangle + u_i' \tag{1.13}$$

where $\langle \cdot \rangle$ denotes an ensemble mean, while u_i' is the fluctuation from the average. It is useful to introduce the variable k' defined as the average Turbulent Kinetic Energy (TKE) [MG17]:

$$k' = \frac{1}{2} \langle u_j' u_j' \rangle \tag{1.14}$$

and, finally, the viscous dissipation ϵ, defined as follows:

$$\begin{aligned} \epsilon &= 2\nu \langle s_{ij} s_{ij} \rangle \\ s_{ij} &= \frac{1}{2} \left(\frac{\partial u_i'}{\partial x_j} + \frac{\partial u_j'}{\partial x_i} \right) \end{aligned} \tag{1.15}$$

Since k' is defined through the velocity fluctuations, it gives a qualitative indication of how much the flow is turbulent. Using the Fourier analysis, it is also possible to obtain the spectrum function E associated with k'. Thus, these two quantities are related by the following equation:

$$k' = \int_0^\infty E(k) dk \tag{1.16}$$

where $k^2 = k_j k_j$, being k_i the wave number vector of Fourier transforms. By analyzing E and its evolution, Kolmogorov was able to find out some general patterns characterizing turbulence at high Reynolds numbers. The three fundamental hypotheses of his theory are the following [Pop00]: first, the small scale turbulent motions are assumed to be statistically isotropic. This statement seems to be reasonable if one considers the theory from Richardson [Ric22]. Indeed, according to his observations, energy is almost entirely dissipated at the smallest scales, so that a cascade occurs which transfers energy from the largest to the smallest ones. Hence, in this process, there must be a loss of information about the domain boundaries, thus leading to the local isotropy. The second hypothesis states that the statistics of the small scale motions are universally and uniquely determined by ν and ϵ. In other words, since any external information is

lost during the cascade, the small scales must be described only in terms of the relevant, local parameters, namely ν and ϵ. Third, the smallest scales are universally and uniquely described by ϵ when k is such that $2\pi/L \ll k \ll 2\pi/\eta$, L being a length scale characterizing the largest turbulent structures. Such range is referred to as the inertial sub-range. Following from the last two hypothesis, there is a unique combination of ν and ϵ to define length, velocity and time scales. These are as follows:

$$\eta = \left(\frac{\nu^3}{\epsilon}\right)^{\frac{1}{4}} \qquad\qquad u_\eta = (\nu\epsilon)^{\frac{1}{4}} \qquad\qquad \tau_\eta = \left(\frac{\nu}{\epsilon}\right)^{\frac{1}{2}} \qquad (1.17)$$

where η in Eq.(1.17) is the Kolmogorov length scale. This last quantity is fundamental, since it represents the typical length scale of the smallest turbulent structures in any flow. Indeed, the most of the dissipation occurs at this scale: this can be seen by computing the local Reynolds number from the parameters in Eq.(1.17), obtaining $Re_\eta = 1$. Under the validity of the above mentioned hypothesis, Kolmogorov derived a universal energy spectrum E for k in the inertial sub-range. This is given by:

$$E(k) = \alpha_K \epsilon^{\frac{2}{3}} k^{-\frac{5}{3}} \qquad (1.18)$$

where α_K is a universal constant.

The assumptions made by Kolmogorov have led to two main results. First, η provides a quantitative estimate of the smallest scales involved in any turbulent flow, thus suggesting a lower limit when creating a mesh for CFD simulations. Second, considering the universality of the energy spectrum in Eq.(1.18), the Kolmogorov's theory opens up the possibility of finding closure models to account for sub-grid scales motions in relatively coarse meshes. As already hinted in the previous section, from this discussion at least two types of simulations follow. On the one hand, Direct Numerical Simulations (DNSs) simulate fluid flows resolving every motion scale down to the Kolmogorov length scale. Hence, DNSs offer the maximum accuracy available, even though with high and often prohibitive computational costs. On the other hand, in Large-Eddy Simulations (LESs), since the mesh size is larger than the Kolmogorov length scale, models are developed in order to consider the contributes coming from the more universal, sub-grid scales.

1.3   Large-eddy simulations

In Large-Eddy Simulations, only a certain range of scales of motions are resolved, while the remaining ones needs to be modelled. This is a consequence of the observations made in the previous section, according to which, while the largest flow structures depend on the specific flow through the boundary constraints, the smallest ones may exhibit a more universal behavior. Considering CFD codes, any discretization procedure implies solving the system of equations on a finite grid of points or cells. As a consequence,

the governing equations are implicitly filtered by the grid, since no sub-grid scale can be resolved. Thus, from a mathematical point of view, the effect of discretization on a generic physical variable ϕ can be seen as that of filtering it with a kernel function G [Pop00]:

$$\bar{\phi}(\mathbf{x}, t) \equiv \int_{\Omega} G(\mathbf{r}, \mathbf{x}) \phi(\mathbf{x} - \mathbf{r}, t) \, d\mathbf{r} \tag{1.19}$$

where Ω represents the entire fluid domain. The kernel function G must satisfy the following normalization condition:

$$\int_{\Omega} G(\mathbf{r}, \mathbf{x}) \, d\mathbf{r} = 1 \tag{1.20}$$

Hence, the original field ϕ is split accordingly:

$$\phi(\mathbf{x}, t) = \bar{\phi}(\mathbf{x}, t) + \phi'(\mathbf{x}, t) \tag{1.21}$$

having defined the residual field as:

$$\phi'(\mathbf{x}, t) \equiv \phi(\mathbf{x}, t) - \bar{\phi}(\mathbf{x}, t) \tag{1.22}$$

The filtering operation defined in Eq.(1.19) is linear and it commutes with time derivatives. Space derivation commutes with $\bar{\cdot}$ only if G does not depend on $\mathbf{x}$, i.e. if G is homogeneous. Even though this is not always true, this last property is assumed to hold in case of implicit filtering. Empirically, the errors deriving from such assumption are relatively small [BH18].

For the sake of simplicity, let us consider the Navier-Stokes equation assuming no gravity force and an incompressible Newtonian fluid with density ρ and kinematic viscosity ν:

$$\frac{\partial u_i}{\partial t} + \frac{\partial u_j u_i}{\partial x_j} = -\frac{\partial p}{\partial x_i} + \frac{\partial}{\partial x_j}\left[\nu \frac{\partial u_i}{\partial x_j}\right] \tag{1.23}$$

where p is the kinematic pressure, defined as $p = P/\rho$, being P the pressure. It is possible to apply the transformation in Eq.(1.19) to u_i and p, obtaining:

$$\frac{\partial \bar{u}_i}{\partial t} + \frac{\partial \bar{u}_j \bar{u}_i}{\partial x_j} = -\frac{\partial \bar{p}}{\partial x_i} + \frac{\partial}{\partial x_j}\left[\nu \frac{\partial \bar{u}_i}{\partial x_j}\right] - \frac{\partial \tau_{ij}^R}{\partial x_j} \tag{1.24}$$

In the last equation, τ_{ij}^R is defined as $\tau_{ij}^R = \overline{u_i u_j} - \bar{u}_i \bar{u}_j$ and is the residual stress tensor. Now, τ_{ij}^R can be decomposed into the sum of an isotropic and anisotropic component:

$$\tau_{ij}^R = \frac{1}{3}\tau_{kk}^R \delta_{ij} + \tau_{ij}^r$$
$$\tau_{ij}^r \equiv \tau_{ij}^R - \frac{1}{3}\tau_{kk}^R \delta_{ij} \tag{1.25}$$

13

Then, by redefining $\bar{p}$ as:

$$\bar{p} + \frac{1}{3}\tau_{kk}^R, \tag{1.26}$$

one gets to the following equation for the filtered velocity:

$$\frac{\partial \bar{u}_i}{\partial t} + \frac{\partial \bar{u}_j \bar{u}_i}{\partial x_j} = -\frac{\partial \bar{p}}{\partial x_i} + \frac{\partial}{\partial x_j}\left[\nu\frac{\partial \bar{u}_i}{\partial x_j}\right] - \frac{\partial \tau_{ij}^r}{\partial x_j} \tag{1.27}$$

Finally, it is useful to introduce the rate of production of residual energy as:

$$P_r = -\tau_{ij}^r \bar{S}_{ij}. \tag{1.28}$$

This quantity indicates how much energy per unit time and unit mass is transferred from the resolved scales down to sub-grid scales.

The Smagorinsky Sub-Grid Scales Model

The system in Eq.(1.27) is not closed and a model is to be provided to compute τ_{ij}^r. Many closure models have been proposed to this end. In the following, the first and most fundamental one, advanced by Smagorinsky [Sma63], is shown. This model is based on the introduction of an eddy turbulent viscosity ν_t, emerging from the residual motions and affecting the resolved ones. The eddy-viscosity hypothesis, introduced by Boussinesq, yields the following linear equation for τ_{ij}^r:

$$\tau_{ij}^r = -2\nu_t \bar{S}_{ij} \tag{1.29}$$

where $\bar{S}_{ij}$ is the filtered strain rate, defined as:

$$\bar{S}_{ij} \equiv \frac{1}{2}\left(\frac{\partial \bar{u}_i}{\partial x_j} + \frac{\partial \bar{u}_j}{\partial x_i}\right) \tag{1.30}$$

Smagorinsky proposed the following model for ν_t:

$$\nu_t = (C_S\Delta)^2\sqrt{2\bar{S}_{ij}\bar{S}_{ij}} \tag{1.31}$$

where C_S is the Smagorinsky coefficient, Δ is the filter width and $C_S\Delta$ represents the Smagorinsky length (l_S). In case of implicit filtering, it is customary to assume $\Delta = \sqrt[3]{V_C}$, where V_C is the cell volume. Using the energy spectrum obtained by Kolmogorov, it can be verified that the Smagorinsky length is actually proportional to Δ when Δ is in the inertial sub-range. In the same context, C_S is estimated to have the value 0.17[3][Lil66]. It must be stressed that this strict proportionality does not hold in general, especially

---

[3]It must be underlined that this is just a theoretical approximated prediction, and that C_S should be tuned depending on the case.

when Δ lies below the inertial range. This causes some issues when considering a wall bounded flow, which will be addressed shortly.

Let us consider the consequences of the Smagorinsky sub-grid model on the momentum equation and on the rate of production of residual energy. Considering the Eq.(1.27), Eq.(1.29) entails:

$$\frac{\partial \bar{u}_i}{\partial t} + \frac{\partial \bar{u}_j \bar{u}_i}{\partial x_j} = -\frac{\partial \bar{p}}{\partial x_i} + \frac{\partial}{\partial x_j}\left[(\nu + \nu_t)\frac{\partial \bar{u}_i}{\partial x_j}\right] \tag{1.32}$$

Hence, it is shown that the sub-grid scale motions affect the resolved ones by increasing the effective viscosity. As far as the energy is concerned, the Eqs.(1.29)-(1.31) imply that there is no energy backscatter from the residual to resolved scales. Indeed, by substituting τ_{ij}^r from Eq.(1.29) in Eq.(1.28), one obtains:

$$P_r = 2\nu_t \bar{S}_{ij}\bar{S}_{ij} \geq 0$$

since $\nu_t \geq 0$ from Eq.(1.31). Thus, P_r is always a sink term for the resolved energy budget.

The Near-Wall Layer

To have a better understanding of the problems occurring in a wall bounded flow, let us briefly introduce the basic properties of boundary layers. When a flow is limited by a smooth wall, the fluid velocity approaches a zero value as the distance from the wall tends to zero. Therefore, considering the case of flat plate channel, the boundary layer may be defined as the region of the fluid domain characterized by velocities lower than their asymptotic value at great distances from the wall. In the following, $\hat{x}$ direction the streamwise direction, while $\hat{y}$ is the wall-normal direction. Near-wall motions are dominated by viscous effects and both the viscosity ν and the wall shear stress τ_w are fundamental parameters. τ_w is defined as:

$$\tau_w = \rho\nu\frac{\partial u_x}{\partial y}\bigg|_{y=0} \tag{1.33}$$

By using ν and τ_w, the characteristic viscous length-scale can be defined:

$$\delta_\nu = \nu\sqrt{\frac{\rho}{\tau_w}} \tag{1.34}$$

Then, the distance from the wall can be measured in units of δ_ν by defining the wall distance y^+:

$$y^+ = \frac{y}{\delta_\nu} \tag{1.35}$$

The wall distance allows for a general analysis of the near-wall region. Indeed, for $y^+ < 50$, in the so-called viscous layer, viscous effects dominate the flow: in particular,

when $y^+ < 5$ (viscous sub-layer) the shear stress is completely dominated by the viscous stresses. On the contrary, when $y^+ > 50$, viscous effects become negligible. In addition, it can be shown that in the near-wall region, the velocity profiles are described by a universal function: this is referred to as the Law of the Wall.

LES-NWR and LES-NWM

Let us turn back to LES simulations. From the previous discussion, in the near-wall region, it follows that the sub-grid model must obey to the constraints imposed by the universal profiles. Thus, two approaches have been developped.

The first one is to resolve down to the smallest, near-wall scales. In this kind of simulations, called LES-NWR (Near-Wall Resolution), the first wall-adjacent cell layer must be within $y^+ \approx 1$, thus resulting in an increase in the computational cost. In addition, a crucial correction is needed in the Smagorinsky model. As already pointed out, the strict proportionality between the Smagorinsky length scale and the Δ is valid in the inertial range only. This is not true in the viscous wall region. Hence, the Smagorinsky length is corrected by the Van Driest dumping function [PM82]:

$$l_S = C_S \Delta \left[1 - exp \left(-y^+/A^+ \right) \right] \tag{1.36}$$

where A^+ is an empirical constant.

The second approach is that of LES-NWM (Near-Wall Model). In this case, the first cell layer is required to be within $y^+ < 300$, thus allowing for coarser meshes in the near-wall region. The main downside of LES-NWM simulation is the need to introduce a model to account for the near-wall processes.

In short, LES simulations share with DNS simulations the ability to simulate transient turbulent flows, even though not every scale of motion is resolved. While this results in less expensive simulations, the filtering operation makes LES strongly dependent on the accuracy of the sub-grid model. Overall, LESs seem to offer a valuable compromise between accuracy and computational costs.

1.4   OpenFOAM

OpenFOAM (OF) is an open source software used to perform computational fluid dynamics simulations. The version employed in the present simulation is OpenFOAM 6, developed and freely distributed by the OpenFOAM Foundation under the General Public License (GPL). Its code is written in C++ programming language, extensively using the object-oriented paradigm and polymorphism. Its versatile algorithms allow the user to tackle quite a wide range of physical and mathematical problems, going from what strictly concerns fluid dynamics (with compressible, incompressible or transonic flows

solvers, for example) to other physical and mathematical problems, such as electromagnetism or financial modelling. In addition, it is also possible to modify the source codes of any solver, so that the customized version best fits for a specific problem. OpenFOAM also provides many utilities for pre-processing, monitoring and post-processing data. As far as pre-processing is concerned, one can find applications for meshing (like blockMesh or snappyHexMesh) or to prepare for a parallel run (like decomposePar). Monitoring can be made at run time through function objects like probes (to sample data in specified positions) or after a solution has been computed. Lastly, post-processing is mainly provided by the postProcess utility, while parallel case reconstruction is accomplished by reconstructPar. The output of an OF simulation can be visualized in Paraview, an open-source data analysis and visualization application, freely distributed by Kitware Inc. under BSD license.

Chapter 2

LES of an anabatic flow in OpenFOAM

2.1 Problem Definition

The present simulation aims to reproduce and analyze an anabatic flow over a smooth, infinite, inclined plane in the presence of a stratified external atmosphere. An LES approach has been considered and validated against the DNS simulation $U30H$ in Giometto et al. [MG17].

    As already underlined in Par.1.2, anabatic flows occur over complex terrains, as the Sun-heated ground surface causes warmer air to ascend along the inclined slope. Hence, such type of flow is deeply dependent on the small-scale, turbulent phenomena taking place within the near-slope boundary layer. In order to obtain a complete e reliable analysis, a LES-NWR approach has been considered. The simulation has been performed using the OpenFOAM 6 software. A detailed description of the case will follow in the next sections. Let us start by introducing the set of governing equations.

2.1.1 Governing Equations

Following [Sch90, EF09, MG17], the problem of anabatic flows can be conveniently described in a rotated frame of reference. For the sake of clarity, let us consider a conventional coordinate system, in which the gravitational acceleration is opposite to the $\hat{z}^*$ direction, and $\hat{x}^*$ and $\hat{y}^*$ lie on a horizontal plane. The smooth, infinitely-extended slope is represented by a plane whose normal vector is inclined by an angle α in the $\hat{x}^*O\hat{z}^*$ plane. An inclined frame of reference can be defined accordingly, so that $\hat{x}$ points into the stream-wise direction, $\hat{y}$ into the span-wise direction, while $\hat{z}$ into the slope-normal direction (see Fig.2.1). Following [Pra42, MG17], the potential temperature θ is decomposed into the sum of the background profile θ^R and its fluctuations θ''. Assuming the
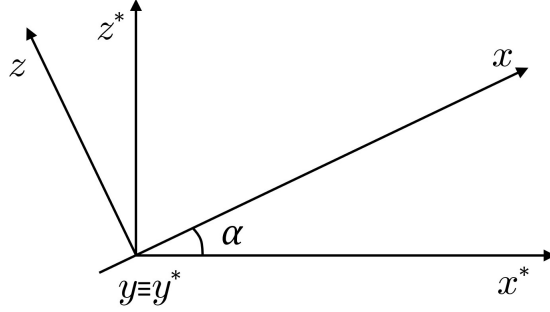
Figure 2.1: Inclined frame of reference

base state to vary linearly with the absolute height z^*, the Brunt-Väisälä frequency is defined as:

$$N \equiv \sqrt{\beta \frac{d\theta^R}{dz^*}} \qquad (2.1)$$

where $\beta \equiv g/\theta_0$, being g the magnitude of the gravity acceleration and θ_0 a reference, constant temperature. The Boussinesq approximation is adopted, so that the density ρ is considered as a constant except when it compares multiplied by g_i. This assumption is valid when the density fluctuations are considerably small. As reported by Ferziger and Perić [3], considering the air, the Boussinesq approximation introduces errors less than 1% for temperature variations of $15K$. In the inclined frame of reference, the momentum, the continuity and the temperature equations can be written as follows:

$$\frac{\partial u_j}{\partial x_j} = 0 \qquad (2.2)$$

$$\frac{\partial u_i}{\partial t} + \frac{\partial u_j u_i}{\partial x_j} = -k_i \beta \theta'' - \frac{\partial \Pi}{\partial x_i} + \frac{\partial}{\partial x_j}\left[\nu \frac{\partial u_i}{\partial x_j}\right] \qquad (2.3)$$

$$\frac{\partial \theta''}{\partial t} + \frac{\partial u_j \theta''}{\partial x_j} = -\frac{\partial u_j \theta^R}{\partial x_j} + \frac{\partial}{\partial x_j}\left[\kappa \frac{\partial \theta''}{\partial x_j}\right] \qquad (2.4)$$

where:

- $k_i = -(sin(\alpha), 0, cos(\alpha))$ is the gravity unit vector;

- $\Pi = (P - \rho_0 g_i x_i)/\rho_0$ is the deviation from the kinematic hydrostatic pressure, being $\rho_0 = \rho(\theta = \theta_0)$;

- ν is the kinematic viscosity;

- κ is thermal diffusivity coefficient.

19

In Eq.(2.4), since θ^R only depends on z^* and $\hat{z}^* = \hat{x}sin\,(\alpha) + \hat{z}cos\,(\alpha)$, the term with θ^R can be computed explicitly. Hence, having defined the buoyancy $b \equiv \beta\theta''$, Eq.s (2.2)-(2.4) are rewritten as:

$$\frac{\partial u_j}{\partial x_j} = 0$$

$$\frac{\partial u_i}{\partial t} + \frac{\partial u_j u_i}{\partial x_j} = -k_i b - \frac{\partial \Pi}{\partial x_i} + \frac{\partial}{\partial x_j}\left[\nu\frac{\partial u_i}{\partial x_j}\right] \tag{2.5}$$

$$\frac{\partial b}{\partial t} + \frac{\partial u_j b}{\partial x_j} = N^2 u_j k_j + \frac{\partial}{\partial x_j}\left[\kappa\frac{\partial b}{\partial x_j}\right]$$

Normalization Procedure

As in [MG17], the following set of typical constant parameters can be defined (respectively, time, length, buoyancy and velocity):

$$T \equiv N^{-1} \qquad L \equiv \frac{|b_S|}{N^2} \qquad B \equiv |b_S| \qquad U \equiv \frac{|b_S|}{N} \tag{2.6}$$

where $b_S > 0$ is the surface buoyancy. Through Eq.(2.6), the following set of dimensionless variables can be introduced:

$$t^\star \equiv t/T \qquad x_i^\star \equiv x_i/L \qquad b^\star \equiv b/B \qquad u_i^\star \equiv u_i/U \qquad \Pi^\star \equiv \Pi/U^2 \tag{2.7}$$

whereby the governing equations are cast in a dimensionless form:

$$\frac{\partial u_j^\star}{\partial x_j^\star} = 0 \tag{2.8}$$

$$\frac{\partial u_i^\star}{\partial t^\star} + \frac{\partial u_j^\star u_i^\star}{\partial x_j^\star} = -k_i b^\star - \frac{\partial \Pi^\star}{\partial x_i^\star} + Gr^{-1/2}\frac{\partial}{\partial x_j^\star}\frac{\partial u_i^\star}{\partial x_j^\star} \tag{2.9}$$

$$\frac{\partial b^\star}{\partial t^\star} + \frac{\partial u_j^\star b^\star}{\partial x_j^\star} = u_j^\star k_j + (Gr^{-1/2}Pr^{-1})\frac{\partial}{\partial x_j^\star}\frac{\partial b^\star}{\partial x_j^\star} \tag{2.10}$$

where $Pr = \nu/\kappa$ is the Prandtl number and the Grashof number has been introduced as $Gr \equiv b_S^4 \nu^{-2} N^{-6}$. As reported in [MG17, FM16], Pr represents the ratio between the the hydrodynamic boundary layer and the thermal boundary layer, while the Grashof number the ratio between buoyancy and viscous forces. For later convenience, it is useful to introduce the conservation equation for the dimensionless turbulent kinetic energy $k'^\star \equiv k'/U^2$. Recalling Eq.(1.13), the conservation equation for $k'^\star$ reads:

$$\frac{\partial k'^\star}{\partial t^\star} + \frac{\partial \langle u_j^\star\rangle k'^\star}{\partial x_j^\star} = -\langle b'^\star u_j'^\star\rangle k_j - \frac{\partial \langle \Pi'^\star u_j'^\star\rangle}{\partial x_j^\star} - \langle u_i'^\star u_j'^\star\rangle\frac{\partial \langle u_i^\star\rangle}{\partial x_j^\star} - \frac{\partial}{\partial x_j^\star}\left(\frac{1}{2}\langle u_i'^\star u_i'^\star u_j'^\star\rangle\right)$$

$$+ Gr^{-1/2}\frac{\partial}{\partial x_j^\star}\frac{\partial k'^\star}{\partial x_j^\star} - Gr^{-1/2}\langle\frac{\partial u_i'^\star}{\partial x_j^\star}\frac{\partial u_i'^\star}{\partial x_j^\star}\rangle \tag{2.11}$$

Given the symmetry of both the equations and the domain, $\langle \cdot \rangle$ can be taken to denote a space-time average on the homogeneity directions (x, y). Thus, it is possible to assume spatial homogeneity on the $\hat{x}$ and $\hat{y}$ directions $(\partial \langle \cdot \rangle / \partial x = \partial \langle \cdot \rangle / \partial y = 0)$ and a zero mean velocity in the $\hat{z}$ direction [MG17]. The dimensionless TKE equation reduces to:

$$\frac{\partial k'^\star}{\partial t^\star} = -\langle b'^\star u_j'^\star \rangle k_j - \frac{\partial \langle \Pi'^\star u_z'^\star \rangle}{\partial z^\star} - \langle u_x'^\star u_z'^\star \rangle \frac{\partial \langle u_x^\star \rangle}{\partial x_z^\star} - \frac{\partial}{\partial z^\star} \left(\frac{1}{2} \langle u_i'^\star u_i'^\star u_z'^\star \rangle \right)$$
$$+ Gr^{-1/2} \frac{\partial^2 k'^\star}{\partial z^{\star 2}} - Gr^{-1/2} \langle \frac{\partial u_i'^\star}{\partial x_j^\star} \frac{\partial u_i'^\star}{\partial x_j^\star} \rangle \tag{2.12}$$

This last equation is used in Giometto et al. [MG17] to compute the TKE budget, and it has been taken as reference so as to reproduce the corresponding terms from the LES.

LES Filtered Equations

Let us turn back to the set of equations in Eq.(2.5). Since OpenFOAM employs dimensioned variables, Eq.(2.5) is taken as the fundamental governing set for the present simulation. As explained in Par.1.3, in the LES approach the Eq.(2.5) is filtered. In the present simulation, a Smagorinsky sub-grid scale model has been employed for the momentum and the buoyancy equation through the use of the Reynolds analogy. Taking into account both the momentum and the continuity equations, the filtered equations read:

$$\frac{\partial \bar{u}_j}{\partial x_j} = 0 \tag{2.13}$$

$$\frac{\partial \bar{u}_i}{\partial t} + \frac{\partial \bar{u}_j \bar{u}_i}{\partial x_j} = -k_i \bar{b} - \frac{\partial \bar{\bar{\Pi}}}{\partial x_i} + \frac{\partial}{\partial x_j} \left[(\nu + \nu_t) \frac{\partial \bar{u}_i}{\partial x_j} \right] \tag{2.14}$$

where the Smagorinsky model has been employed (see Eq.(1.31)), and $\bar{\Pi}$ is redefined as $\bar{\Pi} + 1/3\tau_{kk}^R$, in the same way as in Eq.(1.26). Considering now the buoyancy equation, the filtering operation yields:

$$\frac{\partial \bar{b}}{\partial t} + \frac{\partial \bar{u}_j \bar{b}}{\partial x_j} = N^2 \bar{u}_j k_j + \frac{\partial}{\partial x_j} \left[\kappa \frac{\partial \bar{b}}{\partial x_j} \right] - \frac{\partial B_j}{\partial x_j} \tag{2.15}$$

where $B_i \equiv \overline{bu_i} - \bar{b}\bar{u}_i$ is the analogous of the residual stress tensor (see Eq.(1.25)) and it represents the residual buoyancy flux. In analogy with the Fourier's Law, the hypothesis proposed by Reynolds states:

$$B_i = -\kappa_t \frac{\partial \bar{b}}{\partial x_i} \tag{2.16}$$

where κ_t is the sub-grid thermal diffusion. By substituting the last equation into the filtered buoyancy equation and rearranging the terms on the right-hand side, one obtains:

$$\frac{\partial \bar{b}}{\partial t} + \frac{\partial \bar{u}_j \bar{b}}{\partial x_j} = N^2 \bar{u}_j k_j + \frac{\partial}{\partial x_j} \left[\left(\frac{\nu}{Pr} + \frac{\nu_t}{Pr_t} \right) \frac{\partial \bar{b}}{\partial x_j} \right] \tag{2.17}$$

having defined the turbulent Prandtl number as $Pr_t = \nu_t/\kappa_t$. Hence, the following set of filtered equations can be derived:

$$\frac{\partial \bar{u}_j}{\partial x_j} = 0 \tag{2.18}$$

$$\frac{\partial \bar{u}_i}{\partial t} + \frac{\partial \bar{u}_j \bar{u}_i}{\partial x_j} = -k_i \bar{b} - \frac{\partial \bar{\Pi}}{\partial x_i} + \frac{\partial}{\partial x_j}\left[(\nu + \nu_t)\frac{\partial \bar{u}_i}{\partial x_j}\right] \tag{2.19}$$

$$\frac{\partial \bar{b}}{\partial t} + \frac{\partial \bar{u}_j \bar{b}}{\partial x_j} = N^2 \bar{u}_j k_j + \frac{\partial}{\partial x_j}\left[\left(\frac{\nu}{Pr} + \frac{\nu_t}{Pr_t}\right)\frac{\partial \bar{b}}{\partial x_j}\right] \tag{2.20}$$

The equations from (2.18) to (2.20) represent the actual set of governing equations solved in the OpenFOAM code. For later convenience, it is also useful to introduce the dimensioned conservation equation for the resolved turbulent kinetic energy K. This equation corresponds to Eq.(2.11) for the resolved quantities. Indeed, recalling Eq.(1.13) and Eq.(1.14), K is defined as:

$$K = 1/2\langle \bar{u}'_j \bar{u}'_j \rangle \tag{2.21}$$

where $\bar{u}'_i = \bar{u}_i - \langle \bar{u}_i \rangle$ is the filtered velocity fluctuation. Hence, the conservation equation for K reads:

$$\begin{aligned}
\frac{\partial K}{\partial t} + \frac{\partial \langle \bar{u}_j \rangle K}{\partial x_j} = &-\langle \bar{b}' \bar{u}'_j \rangle k_j - \frac{\partial \langle \bar{\Pi}' \bar{u}'_j \rangle}{\partial x_j} - \langle \bar{u}'_i \bar{u}'_j \rangle \frac{\partial \langle \bar{u}_i \rangle}{\partial x_j} - \frac{\partial}{\partial x_j}\left(\frac{1}{2}\langle \bar{u}'_i \bar{u}'_i \bar{u}'_j \rangle\right) \\
&+ \frac{\partial}{\partial x_j}\left[(\nu + \nu_t)\frac{\partial K}{\partial x_j}\right] - (\nu + \nu_t)\langle \frac{\partial \bar{u}'_i}{\partial x_j}\frac{\partial \bar{u}'_i}{\partial x_j} \rangle
\end{aligned} \tag{2.22}$$

Again, considering the symmetry of the problem, the last equation reduces to the following:

$$\begin{aligned}
\frac{\partial K}{\partial t} = &-\langle \bar{b}' \bar{u}'_j \rangle k_j - \frac{\partial \langle \bar{\Pi}' \bar{u}'_z \rangle}{\partial z} - \langle \bar{u}'_x \bar{u}'_z \rangle \frac{\partial \langle \bar{u}_x \rangle}{\partial z} - \frac{\partial}{\partial z}\left(\frac{1}{2}\langle \bar{u}'_i \bar{u}'_i \bar{u}'_z \rangle\right) \\
&+ \frac{\partial}{\partial z}\left[(\nu + \nu_t)\frac{\partial K}{\partial z}\right] - (\nu + \nu_t)\langle \frac{\partial \bar{u}'_i}{\partial x_j}\frac{\partial \bar{u}'_i}{\partial x_j} \rangle
\end{aligned} \tag{2.23}$$

2.1.2 Geometry and Mesh

Following [MG17], the set of governing equations has been integrated using a regular domain with normalized dimensions $[0, 0.241] \times [0, 0.241] \times [0, 0.324]$. For the sake of clarity, the slope surface will be referred to as the floor, while the upper face, opposite to the floor, as the ceiling. A static, structured, orthogonal mesh has been produced using the blockMesh utility in OF. The grid is $96 \times 96 \times 256$ cells in the three directions, and it is shown in Fig.2.2. A hyperbolic stretching has been performed on the $\hat{z}$ direction, so that the mesh is mostly refined in the floor's proximity. The stretching parameters have been tuned considering as reference the grid proposed in [MG17]. In particular, the
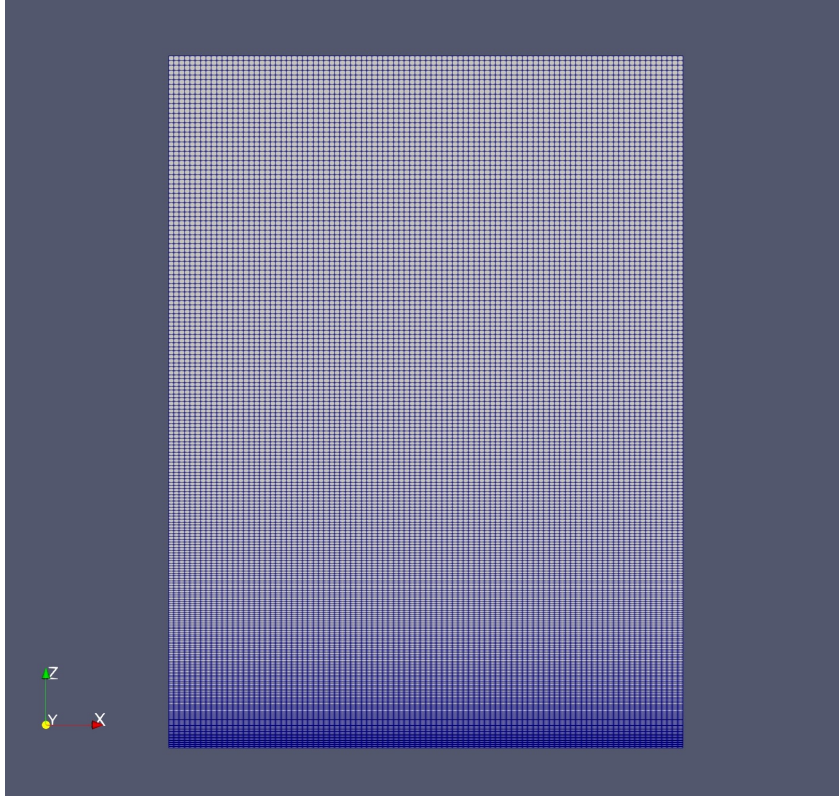
Figure 2.2: Mesh adopted in the present simulation displaying the stretching along the vertical direction.

height of first layer of cells next to the floor has been taken to be equal to that employed in the DNS by Giometto et al. Since for the DNS a $384 \times 384 \times 1032$ grid was employed, the mesh adopted in the present simulation is considerably smaller, having $\approx 98\%$ less cells.

2.1.3 Simulation

The case has been set up considering a $\alpha = 30°$ inclined slope, for a fluid with kinematic viscosity $\nu = 1.5 \times 10^{-5} m^2/s$. The surface buoyancy has been $b_S = 1m/s^2$, while the Prandtl number $Pr = 1$. The Brunt-Väisälä frequency N has been conveniently chosen in order to obtain a Grashof number $Gr = 2.1 \times 10^{11}$, equal to the one employed in [MG17]. Thus, the adopted value has been $N \cong 0.526 s^{-1}$. A sponge region has been applied the top 15% of the domain, so as to avoid internal-waves reflection and a non-physical accumulation of turbulent kinetic energy in the upper part of the domain.

Considering the laminar counterpart of this case, it can be demonstrated that $\langle u_x \rangle$ and $\langle b \rangle$ represent a set of coupled oscillators, whose period is given by $T_p = 2\pi/N sin(\alpha)$

[McN82]. Hence, as proposed in [MG17], the total run time T_{max} has been set equal to $6T_p$. The statistics have been computed only in the last $3T_p$, discarding the first 3 periods to allow the flow to develop and to approach a statistical steady-state configuration. Table 2.1 reports the characteristic parameters of the simulation.

T_{max}/T	α [°]	$\nu\,[m^2/s]$	$b_S\,[m/s^2]$	$N\,[s^{-1}]$	Gr
24π	30	1.5×10^{-5}	1	0.526	2.1×10^{11}

Table 2.1: Set of parameters employed in the simulation.

The boundary conditions employed are presented in Tab.2.2. Since the fluid starts from rest, as initial condition, a zero-value has been set in the internal fluid domain for all the fields.

face	$\bar{u}_i$	$\bar{b}$	$\bar{\Pi}$	$\bar{\nu}_t$	$\bar{\kappa}_t$
floor	$\bar{u}_i = 0$	$\bar{b} = b_S$	zero-gradient	zero-gradient	zero-gradient
ceiling	zero-gradient	$\bar{b} = 0$	$\bar{\Pi} = 0$	zero-gradient	zero-gradient
vertical faces	cyclic	cyclic	cyclic	cyclic	cyclic

Table 2.2: Boundary conditions. Here, "zero-gradient" indicates a standard Neumann condition, in which the face-normal gradient is set to zero.

The simulation has been performed in OpenFOAM 6 and the solver has been adapted from buoyantBoussinesqPimpleFoam, included in the official release. The most relevant changes have been brought to the files for the momentum (UEqn.H) and the temperature equations (TEqn.H, renamed as bEqn.H), with a modification in the pressure file (pEqn.H) for consistency. For the sake of brevity, the files UEqn.H and bEqn.H are entirely reported in the following, while the change in pEqn.H is only mentioned. Starting from the momentum equation, the pressure decomposition originally included in the solver has been modified. In the previous version the solved pressure (named p_rgh) was defined as follows:

$$\text{p\_rgh} = \left(P - \rho g_i x_i\right)/\rho_0 \tag{2.24}$$

where P is the pressure and ρ is the density, a linear function of the temperature in the Boussinesq approximation. Therefore, the original Navier-Stokes equation was as

24

follows:

$$\frac{\partial u_i}{\partial t} + \frac{\partial u_j u_i}{\partial x_j} = -\frac{\partial \text{p\_rgh}}{\partial x_i} + \frac{\partial}{\partial x_j}\left[\nu \frac{\partial u_i}{\partial x_j}\right] + k_j x_j \frac{\partial b}{\partial x_i} \quad (2.25)$$

where b is the buoyancy. In the last equation, the last term on the right-hand side is explicitly dependent on the position. Considering the frame of reference defined in Par.2.1.1, it is found that two points at the same height (i.e. same z values) located on opposite vertical faces, exhibit different $k_j x_j$ values, whose difference is $|\Delta(k_j x_j)| = sin(\alpha)L_x$, being L_x the domain length in the $\hat{x}$ direction. Therefore, since the position-dependent term appears in the momentum equations [PO01], cyclic conditions on vertical boundaries lead to unphysical solutions. Hence, the following pressure decomposition has been introduced:

$$\text{p\_rgh} = (P - \rho_0 g_i x_i)/\rho_0 \quad (2.26)$$

Indeed, this last definition coincides with that of Π (see Eq.(2.3)). In this case, as shown in List 2.1 at line 29, no position-dependent term is needed, allowing for cyclic boundary conditions. The pressure file pEqn.H has been modified accordingly, removing the term "phig" from line 6. The transposition of Eq.(2.19) into the UEqn.H file has been completed by adding the buoyancy source term (List 2.1, line 12).

```
1     // Solve the momentum equation
2
3     MRF.correctBoundaryVelocity(U);
4
5     fvVectorMatrix UEqn
6     (
7         fvm::ddt(U)
8       + fvm::div(phi, U)
9       + MRF.DDt(U)
10      + turbulence->divDevReff(U)
11     ==
12      - b*k
13      + fvOptions(U)
14     );
15
16     UEqn.relax();
17
18     fvOptions.constrain(UEqn);
19
20     if (pimple.momentumPredictor())
21     {
22         solve
23         (
24             UEqn
25          ==
26             fvc::reconstruct
27             (
28                 (
```

```
29  //                    - khf*fvc::snGrad(rhok)
30                        - fvc::snGrad(p_rgh)
31                  )*mesh.magSf()
32             )
33        );
34
35        fvOptions.correct(U);
36     }
```

Listing 2.1: UEqn.H

Taking into account the buoyancy file, the velocity source term appearing in Eq.(2.20) has been included (see List 2.2, lines 14-15), so as to account for the background stratification. A mixed implicit-explicit configuration has been adopted: the purpose of this solution is to increase the diagonal dominance of the solution matrix, thus making it numerically more stable [Gre15].

```
1  {
2      alphat = turbulence->nut()/Prt;
3      alphat.correctBoundaryConditions();
4
5      volScalarField alphaEff("alphaEff", turbulence->nu()/Pr + alphat);
6      volScalarField source("source", N2*(U & k) );
7
8      fvScalarMatrix bEqn
9      (
10         fvm::ddt(b)
11       + fvm::div(phi, b)
12       - fvm::laplacian(alphaEff, b)
13      ==
14         fvm::Sp(four*source,b)        // implicit-
15       + source*(1.0-four*b)          // -explicit source term
16       + fvOptions(b)
17     );
18
19     bEqn.relax();
20
21     fvOptions.constrain(bEqn);
22
23     bEqn.solve();
24
25     //radiation->correct();              -> Not necessary in this case
26
27     fvOptions.correct(b);
28  }
```

Listing 2.2: bEqn.H

Using the OpenFOAM nomenclature, the numerical schemes adopted are summarised in the following list:

26

- time derivatives: backward scheme (already presented as the SOUE scheme in Eq.(1.10));

- gradients: Gauss integration with linear interpolation;

- divergences: Gauss integration with linear interpolation;

  velocity advection: bounded Gauss integration with the Gamma scheme (the limit has been 0.2);

  buoyancy advection: Gauss integration with MUSCL scheme;

- laplacians: Gauss integration with linear interpolation

- interpolations: linear scheme

Given the orthogonality of the mesh, orthogonal corrections do not affect the present simulation. An overall second-order accuracy has been maintained.

2.2 Results

In this section the results from the present LES simulation are shown. Let us recall that, in what follows, $\langle \cdot \rangle$ indicates a space-time average on the homogeneity directions (x, y), and that only the last $3T_p$ time periods have been employed. Also, all the quantities are normalized using the set of parameters defined in Eq.(2.6). When considering the vertical profiles, a dotted horizontal line is used to mark the lower boundary of the sponge layer. Let us start by taking into account the comparison between the results from the present LES and the DNS solution shown in [MG17]. The latter has been graphically acquired from the figures reported in the article, hence the uncertainty deriving from this method is to be taken into account.

Mean Quantities

In Fig.2.3a and Fig.2.3b, respectively, the vertical profiles of the normalized stream-wise velocity and the normalized mean buoyancy are shown. Qualitatively, the LES velocity profile shows a satisfactory agreement with the results from the DNS. The back-flow region around $z/L \approx 10^{-1}$ and the near-wall region below $z/L \approx 10^{-3}$ are well reproduced, though $\langle \bar{u}_x \rangle / U$ is underestimated in the LES in the region in between. In particular, the position of the maximum and the profile's shape in its proximity do not fit at best with the DNS profile. This may be explained by an excessive dissipation of the Smagorinsky sub-grid scale model in this region. Considering Fig.2.3b, the normalized mean buoyancy profile is well reproduced. Three distinct zones can be identified and some correspondences can be found with the stream-wise velocity vertical profile.

- The near-wall region below $z/L \approx 3 \cdot 10^{-3}$ is characterized by an approximately exponential mean buoyancy profile, which tends to b_S approaching the floor. In this layer, a corresponding increase in the mean stream-wise velocity can be outlined, thus verifying the correlation between positive buoyancy values and an the flow development.

- An intermediate region can be found from $z/L \approx 3 \cdot 10^{-3}$ up to $z/L \approx 6 \cdot 10^{-2}$ in which the buoyancy decrease is less intense, capped above by a local, slightly negative buoyancy minimum. This is the region were the flow is fully developed, as shown in the mean velocity vertical profile.

- In the outer layer, the buoyancy remains constant at a zero-value, with a corresponding stable zero-value for the stream-wise mean velocity.

Figures 2.4a and 2.4b superpose the profiles obtained through the one-dimensional, laminar model first proposed by Prandtl [Pra42] (in this case, a linear scale on the vertical axis is used). This simplified approach provides an analytic expression for both the stream-wise velocity and the buoyancy as a function of the normalized height. The solution obtained by Prandtl (also referred to as the constant-K solution), using the dimensionless parameters introduced in Eq.(2.7), is as follows [MG17]:

$$u^{\star} = -b_S Pr^{-1/2} sin(\sigma z^{\star}) exp(-\sigma z^{\star}) \qquad\qquad z^{\star} \in [0, \infty[\qquad\qquad (2.27)$$
$$b^{\star} = b_S cos(\sigma z^{\star}) exp(-\sigma z^{\star}) \qquad\qquad z^{\star} \in [0, \infty[\qquad\qquad (2.28)$$

where $\sigma = (GrPr^{-1})^{1/4}(sin(\alpha))^{1/2}$. In Eq.(2.27), the normalized one-dimensional velocity $u^{\star}$ corresponds to the normalized mean stream-wise velocity, thus allowing for a direct comparison. Taking into account Fig.2.4b, the Prandtl's solution is characterized by a narrower region with fully developed flow and the negative-buoyancy region is predicted to be at a lower height. Considering the results in Fig.2.4a, it is apparent that the constant-K solution displays considerably higher stream-wise velocity values, showing the fundamental influence of the turbulent phenomena for this case. Despite that, the constant-K solution is still able to reproduce the height of the maximum velocity quite faithfully. Also, the possibility to find an analytic solution for a laminar anabatic flow, still provides a useful and straightforward tool to guide to the interpretation of the phenomenon.

Standard Deviations and Turbulent Kinetic Energy

In Fig.2.5a the vertical profile of the normalized velocity root-mean square (RMS) for each component is displayed, showing a good agreement with the DNS data. The discrepancies between the data sets can be described as follows. In the LES, both the RMSs of the x and the y velocity components are underestimated roughly from $z/L \approx 3 \times 10^{-3}$
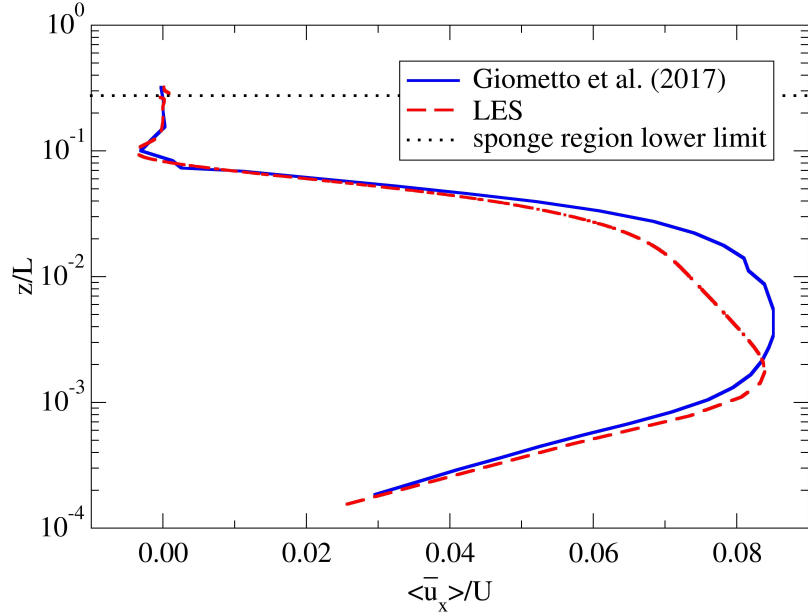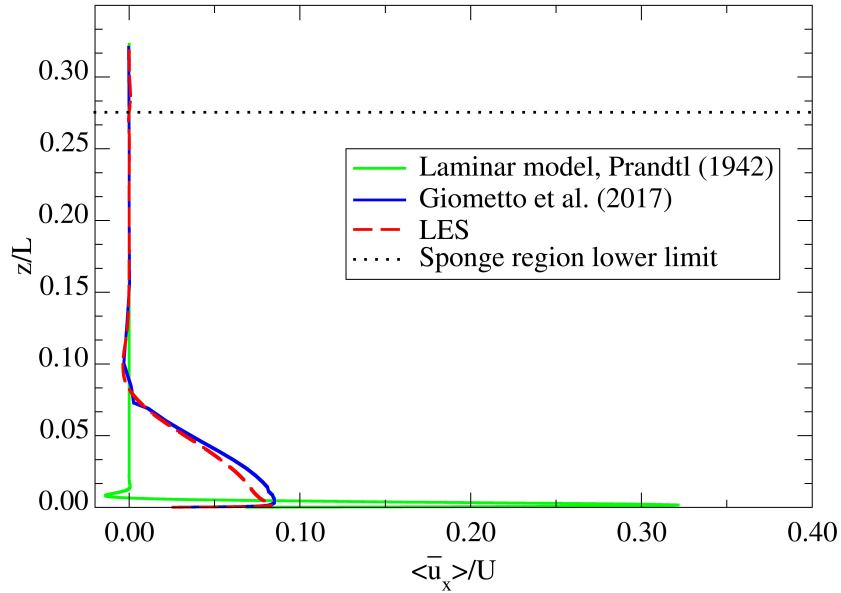
(a) Normalized mean streamwise velocity vertical profiles. Comparison between the results from the present simulation and those from the DNS U30H in Giometto et al. (DNS data do not represent resolved quantities).
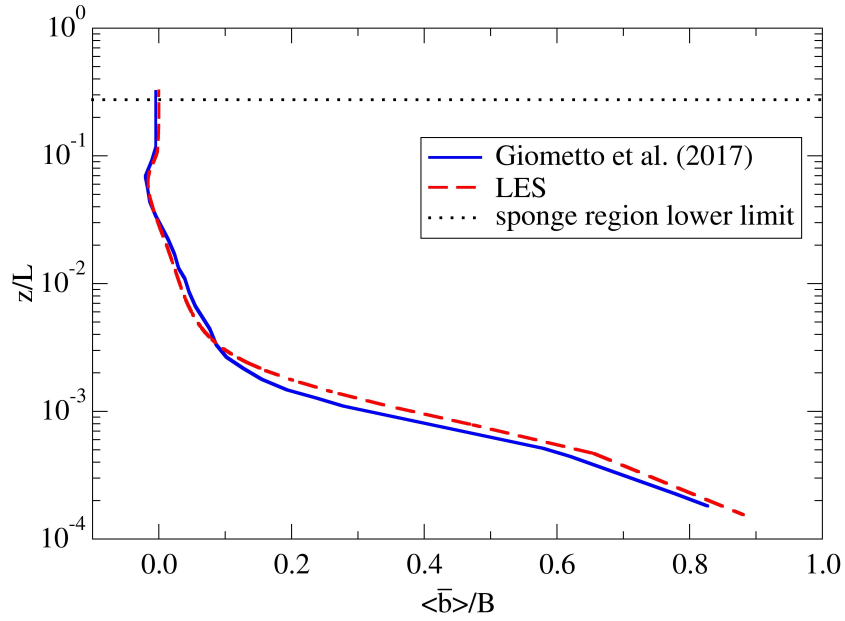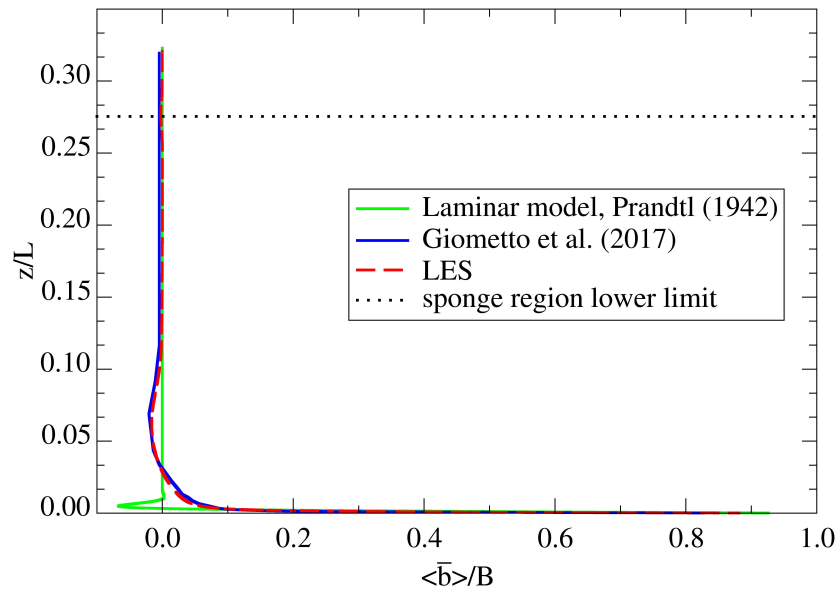

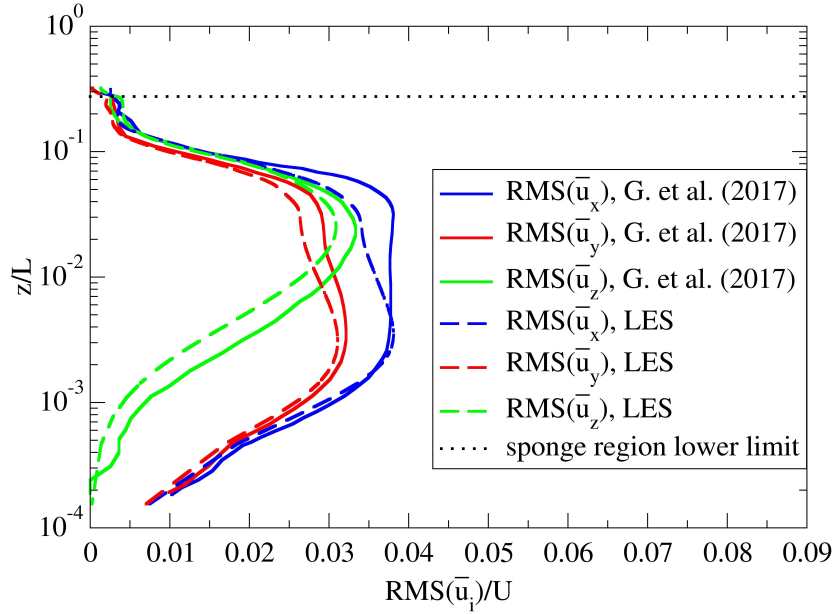(b) Normalized mean buoyancy vertical profiles. Comparison between the results from the present simulation and those from the DNS U30H in Giometto et al. (DNS data do not represent resolved quantities).

(a) Normalized mean streamwise velocity vertical profiles (linear scale on the vertical axis). Comparison between the results from the present simulation, the profile from the laminar solution by Prandtl and those from the DNS U30H in Giometto et al. (DNS data do not represent resolved quantities).

(b) Normalized mean buoyancy vertical profiles (linear scale on the vertical axis). Comparison between the results from the present simulation, the profile from the laminar solution by Prandtl and those from the DNS U30H in Giometto et al. (DNS data do not represent resolved quantities).

to $z/L \approx 8 \times 10^{-2}$, while the z component shows a stable underestimate in the near-wall region, approximately below $z/L \approx 5 \times 10^{-2}$. Such deviations may be explained by an excess in the TKE dissipation caused by the Smagorinsky model, in the same manner as for the case of the mean velocity profiles. It is worth noting the differences characterizing the relative importance of the three components in the near-wall region. In particular, the standard deviation of the z component is considerably smaller than that in the x and y directions, in accordance with the turbulence anisotropy, which will be shown later in the scatter plots.

It is also customary to report the TKE vertical profile. This is displayed in Fig.2.5b. As a consequence of the already mentioned discrepancies shown by the velocity standard deviations, the TKE values are underestimated in the intermediate region, from $z/L \approx 2 \times 10^{-3}$ to $z/L \approx 7 \times 10^{-2}$, whereas a good agreement can be found in the other regions. Considering the vertical profile of the normalized buoyancy standard deviation in Fig.2.6, the data from LES correctly reproduce the DNS profile in the outer part of the domain (above $z/L \approx 1.6 \times 10^{-3}$), where the RMS exhibits a marked maximum value. In the near wall region, the buoyancy standard deviation is constantly underestimated, thus probably showing issues in the near-wall modelling of the turbulence. Indeed, in the present simulation, the turbulent thermal diffusivity is taken to be proportional to the turbulent kinematic viscosity by means of the constant turbulent Prandtl number (see Eq.(2.20)). Therefore, an excess in the dissipation caused by the Smagorinsky model results in an overestimate of the buoyancy turbulent diffusion, thus possibly explaining lower values in the near-wall buoyancy standard deviation.

Turbulent Fluxes

Taking into account the turbulent fluxes, the normalized vertical momentum and buoyancy fluxes are shown, respectively, in Fig.2.7a and Fig.2.7b. Considering the vertical momentum flux in Fig.2.7a, the results from the LES reproduce the DNS data quite accurately, only slightly underestimating the maximum value. The profiles in the figure show a net upward turbulent diffusion of momentum, thus proving the active role played by turbulence in the overall statistical stationary equilibrium. Turning to the buoyancy flux in 2.7b, it can be seen to be underestimated in the inner regions for $z/L < 2.5 \times 10^{-2}$, while in the outer layers the agreement is good. Similarly to the vertical momentum flux, a significant upward buoyancy diffusion characterizes the inner regions, while a non-negligible negative buoyancy flux layer can be found from $z/L \approx 6 \times 10^{-2}$ to $z/L \approx 1.3 \times 10^{-1}$. In addition, the mean buoyancy flux can be commented by means of the gradient-diffusion hypothesis [Pop00]. For a scalar ϕ, it reads:

$$\langle \bar{u}_i' \bar{\phi}' \rangle = -\Gamma_T \frac{\partial \langle \bar{\phi} \rangle}{\partial x_i} \tag{2.29}$$

(a) Normalized velocity standard deviations vertical profiles. Comparison between the results from the present simulation and those from the DNS U30H in Giometto et al. (DNS data do not represent resolved quantities).
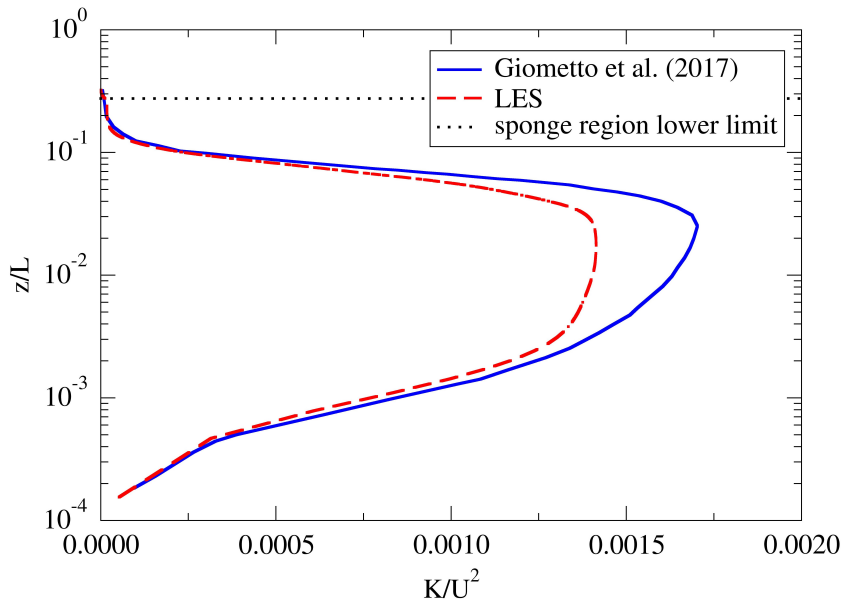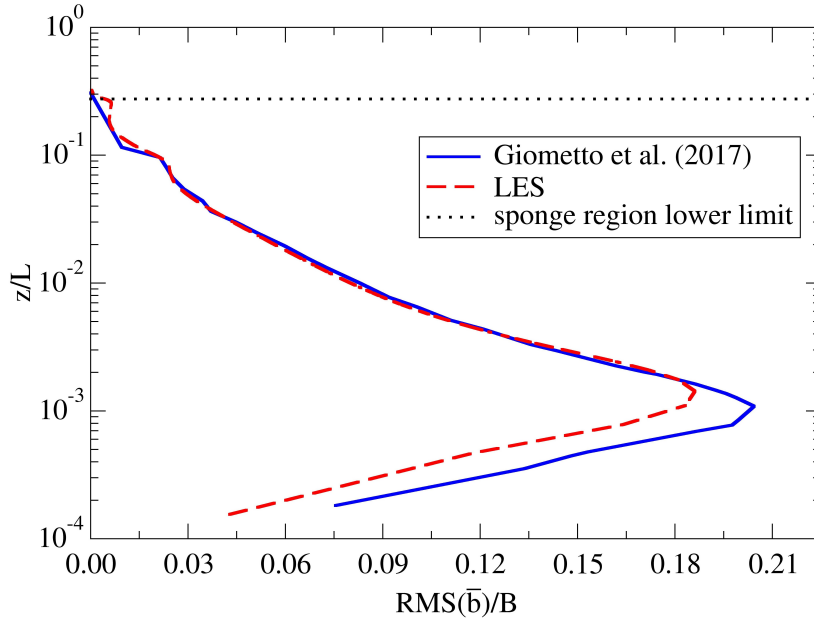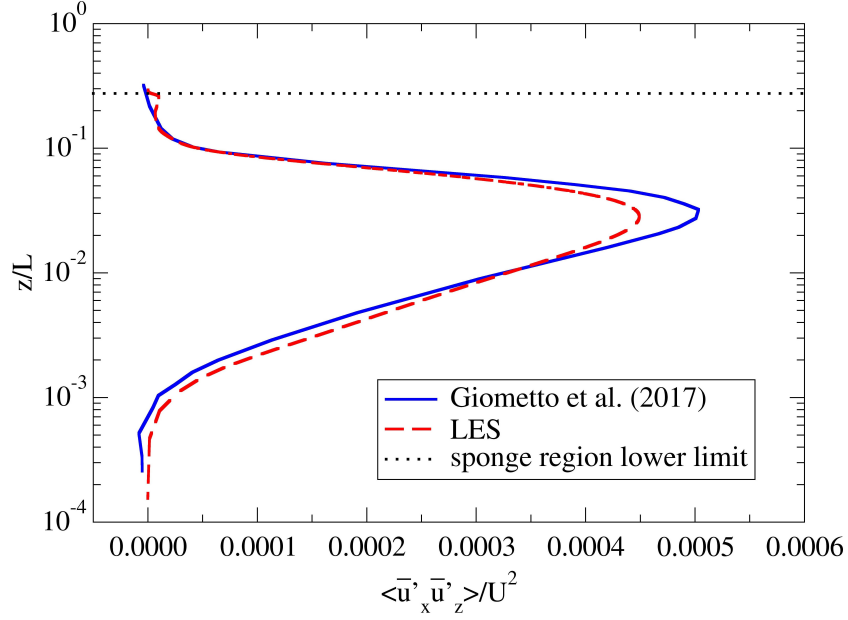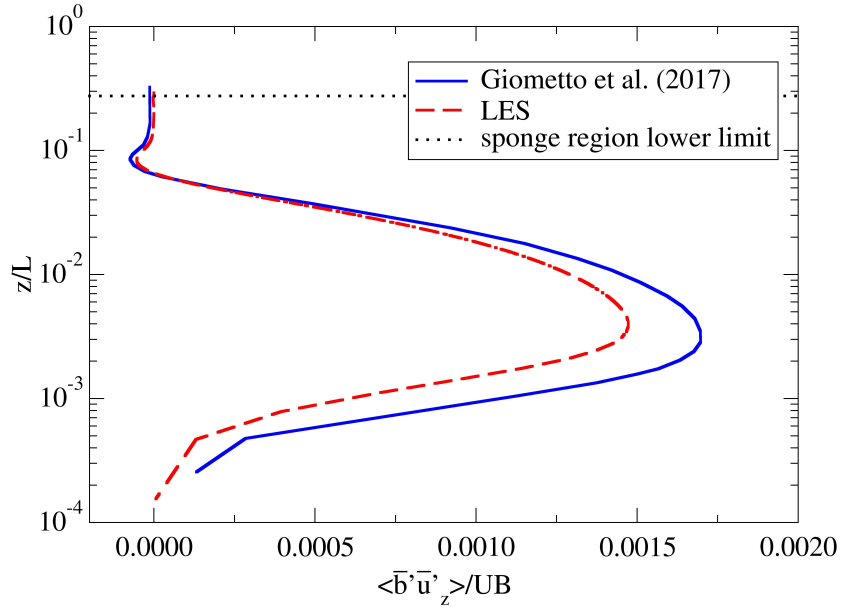

(b) Normalized K vertical profile. Comparison between the results from the present simulation and those from the DNS U30H in Giometto et al. (DNS data do not represent resolved quantities).

Figure 2.6: Normalized buoyancy standard deviation vertical profiles. Comparison between the results from the present simulation and those from the DNS U30H in Giometto et al. (DNS data do not represent resolved quantities).

where primes indicate fluctuations from mean values (in the sense of Reynolds decompositions) and Γ_T is a scalar representing the turbulent diffusivity. The gradient-diffusion hypothesis can be used to make a crossed comparison between the computed mean buoyancy flux and its mean vertical profile. Since spatial derivatives of mean values in the homogeneity directions are null, the gradient-diffusion hypothesis for the buoyancy reads as follows:

$$\langle \bar{u}_z' \bar{b}' \rangle = -\Gamma_T \frac{\partial \langle \bar{b} \rangle}{\partial z} \tag{2.30}$$

As a consequence, stationary points for the mean buoyancy profile are expected in correspondence with zero values in the buoyancy vertical flux. This is confirmed by the results, since a minimum in the mean buoyancy can be found at $z/L \cong 6.5 \times 10^{-2}$, where the buoyancy vertical flux crosses a zero value.

(a) Normalized $\langle \bar{u}'_x \bar{u}'_z \rangle$ vertical profile. Comparison between the results from the present simulation and those from the DNS U30H in Giometto et al. (DNS data do not represent resolved quantities).

(b) Normalized $\langle \bar{b}' \bar{u}'_z \rangle$ vertical profile. Comparison between the results from the present simulation and those from the DNS U30H in Giometto et al. (DNS data do not represent resolved quantities).

Turbulent Kinetic Energy Budget

The turbulent kinetic budget resulting from Eq.(2.23) is reported here for convenience:

$$
\begin{aligned}
\frac{\partial K}{\partial t} = & - \langle \bar{b}' \bar{u}'_j \rangle k_j - \frac{\partial \langle \bar{\Pi}' \bar{u}'_z \rangle}{\partial z} - \langle \bar{u}'_x \bar{u}'_z \rangle \frac{\partial \langle \bar{u}_x \rangle}{\partial z} - \frac{\partial}{\partial z} \left(\frac{1}{2} \langle \bar{u}'_i \bar{u}'_i \bar{u}'_z \rangle \right) \\
& + \frac{\partial}{\partial z} \left[(\nu + \nu_t) \frac{\partial K}{\partial z} \right] - (\nu + \nu_t) \langle \frac{\partial \bar{u}'_i}{\partial x_j} \frac{\partial \bar{u}'_i}{\partial x_j} \rangle
\end{aligned}
\tag{2.31}
$$

Focusing on the production and destruction of TKE, it is useful to define the following terms [MG17]:

$$
\begin{aligned}
P_s &\equiv - \langle \bar{u}'_x \bar{u}'_z \rangle \frac{\partial \langle \bar{u}_x \rangle}{\partial z} \\
P_{b,1} &\equiv \langle \bar{b}' \bar{u}'_x \rangle sin(\alpha) \\
P_{b,3} &\equiv \langle \bar{b}' \bar{u}'_z \rangle cos(\alpha) \\
\epsilon &\equiv - (\nu + \nu_t) \langle \frac{\partial \bar{u}'_i}{\partial x_j} \frac{\partial \bar{u}'_i}{\partial x_j} \rangle
\end{aligned}
\tag{2.32}
$$

where P_s is the shear production of TKE, $P_{b,1}$ and $P_{b,3}$ account for the buoyant production of TKE, and ϵ represents the viscous dissipation. In this case, when computing ϵ, the turbulent viscosity ν_t has been added to ν, so as to correct the filtered quantities to include the sub-grid effects. The comparison between the terms obtained with the LES and those from the DNS is shown in Fig.2.8. Both the buoyant production terms exhibit a good agreement with the DNS data. The shear production term is quite accurately reproduced in the outer layer, whereas in the inner region it presents some discrepancies. In particular, in the intermediate layer the LES overestimates P_s, while in the near-wall region this term is underestimated (or overestimated, considering its absolute value). The viscous dissipation shows discrepancies in the entire profile, exhibiting larger values (smaller, if the absolute value is considered) in most of the domain height, while peaking with a more negative value only at the point closest to the wall. Especially for the viscous dissipation term, further investigation is needed. Overall, the TKE budget from LES confirms the following main features, as reported in [MG17]. It is verified in the LES the importance of both the buoyant production terms, which are the most relevant ones for the production of TKE in the intermediate and inner layers. It is confirmed that both these terms take only positive values, in fact representing production terms. Considering the shear production P_s, a negative-value region is reproduced in the upper part of the near-wall layer, verifying the presence of a sink of TKE due to the shear stress. This implies a reversed energy transfer from the turbulence to the mean flow. A positive peak in P_s is correctly shown in the outer region, where the shear production becomes the leading term. The small, positive maximum in the near wall region is not reproduced by the LES.
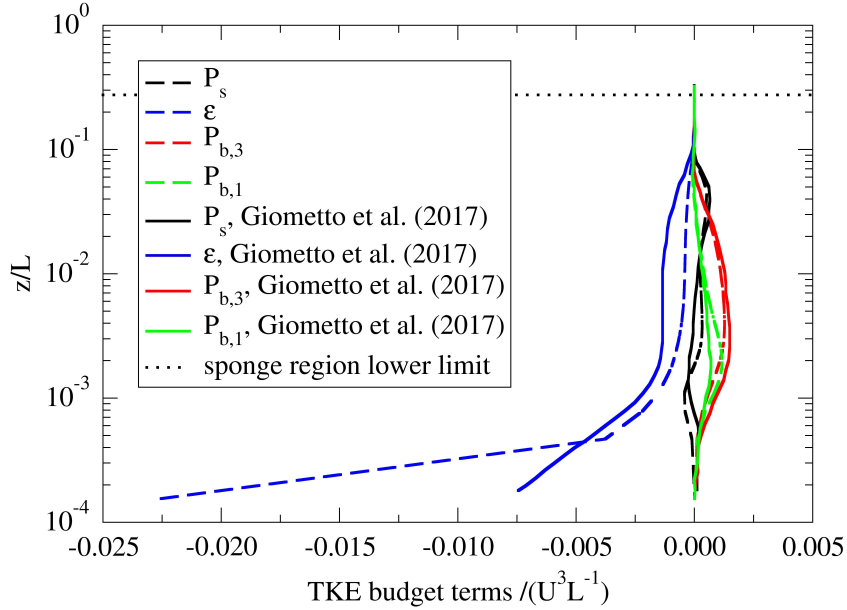
Figure 2.8: Vertical profile of the normalized turbulent kinetic budget. Comparison between the results from the present simulation and those from the DNS U30H in Giometto et al. (DNS data do not represent resolved quantities).

Anisotropy of the Turbulence

Let us now evaluate the anisotropy characterizing the turbulence. This is achieved through the scatter plots in Fig.2.9a to Fig.2.9d. The x and z components of the velocity fluctuations have been computed at fixed positions considering a subset of the computed time steps and using the output from the probes functions, available in OpenFOAM. Such positions have been taken on the vertical of the domain centre (here, the centre is taken on a $\hat{x}O\hat{y}$ plane). The points have been fixed prior to starting the simulation by checking the figures shown in [MG17] and considering heights corresponding to relevant flow features. The following z/L values have been chosen: $z/L = 10^{-3}$, $z/L = 4 \times 10^{-3}$, $z/L = 10^{-2}$ and $z/L = 10^{-1}$, corresponding, respectively, to the Fig.2.9a, Fig.2.9b, Fig.2.9c and Fig.2.9d. The first point ($z/L = 10^{-3}$) is located in the near-wall region, where the flow is almost fully developed and the velocity standard deviations in the same x and z directions are markedly different. A strong anisotropy can be seen in Fig.2.9a. The second one ($z/L = 4 \times 10^{-3}$, Fig.2.9b) lies in the transition between the near-wall and the intermediate layers and it is characterized by a fully developed flow and a still remarkable anisotropy. Considering the third point ($z/L = 10^{-2}$, Fig.2.9c), located in the back-flow zone, the flow exhibits a less intense anisotropy, in accordance with a lower difference in the RMS values of the x and z velocity components. The last figure ($z/L = 10^{-1}$, Fig.2.9d) corresponds to the point positioned in the outer region. While

36

this figure confirms the general trend of decreasing anisotropy at increasing heights, it also shows an interesting deviation in the z component of the velocity. Indeed, such behavior is explained by visualizing a vertical section of the fluid domain passing through the probe point.

Figures 2.10a and 2.10b show the velocity magnitude (colour plot) and the velocity projection on that plane (arrow plot), considering two time instants selected in proximity of the above mentioned fluctuation (in these figures and in the following one, only the lower part of the domain is visualized). By looking in a neighborhood of the probe point (in the figure, marked with a red dot), it is apparent that the deviation observed in the vertical component of the velocity is caused by the transit of an upward plume. It can be also shown that the plume in Fig.2.10a is a turbulent one, thus direct responsible of the transport of TKE. Indeed, as displayed in Fig.2.11a, a notable increase in the turbulent kinetic energy is co-located with the upward structure in Fig.2.10a.

Vertical Sections of the Instantaneous Fields

In Fig.2.12, plots of instantaneous fields are collected. In the top-right and bottom-left panels, respectively, the x and z velocity components are shown. In the former, an instantaneous back-flow region can be seen at approximately $z/L \approx 0.1$, in accordance with the mean behavior shown in Fig.2.3a, while, in the latter, both upward and downward flows characterize the vertical section. The same upward flows (indeed organized in plumes), are displayed in the bottom-right 3D plot, showing the 3-dimensional shape of these flow structures.

ν_t/ν Ratio

Figure 2.13 displays the ratio between the kinematic turbulent viscosity ν_t and the kinematic viscosity ν. Overall, the ratio remains below 0.4, thus showing that the performed LES simulation is well resolved. In addition, this figure allows to visualize the sharp damping effect induced by the Van Driest correction to the cube-root grid size Δ. By decreasing the distance from the floor, a certain height is reached at which the Δ value becomes greater than that computed with the Van Driest correction. Hence, below this point, the Van Driest damping is adopted, so as to guarantee a zero-valued turbulent viscosity on the floor.

Summary

The results from the LES simulation have been compared with DNS data reported in [MG17], showing an overall good agreement. Some discrepancies have been noted in the vertical mean profiles and in the RMS values, often characterized by underestimates. Such behavior may be explained by an excess in the dissipation caused by the Smagorinsky model, especially in the near-wall region. As far as the viscous dissipation ϵ, some
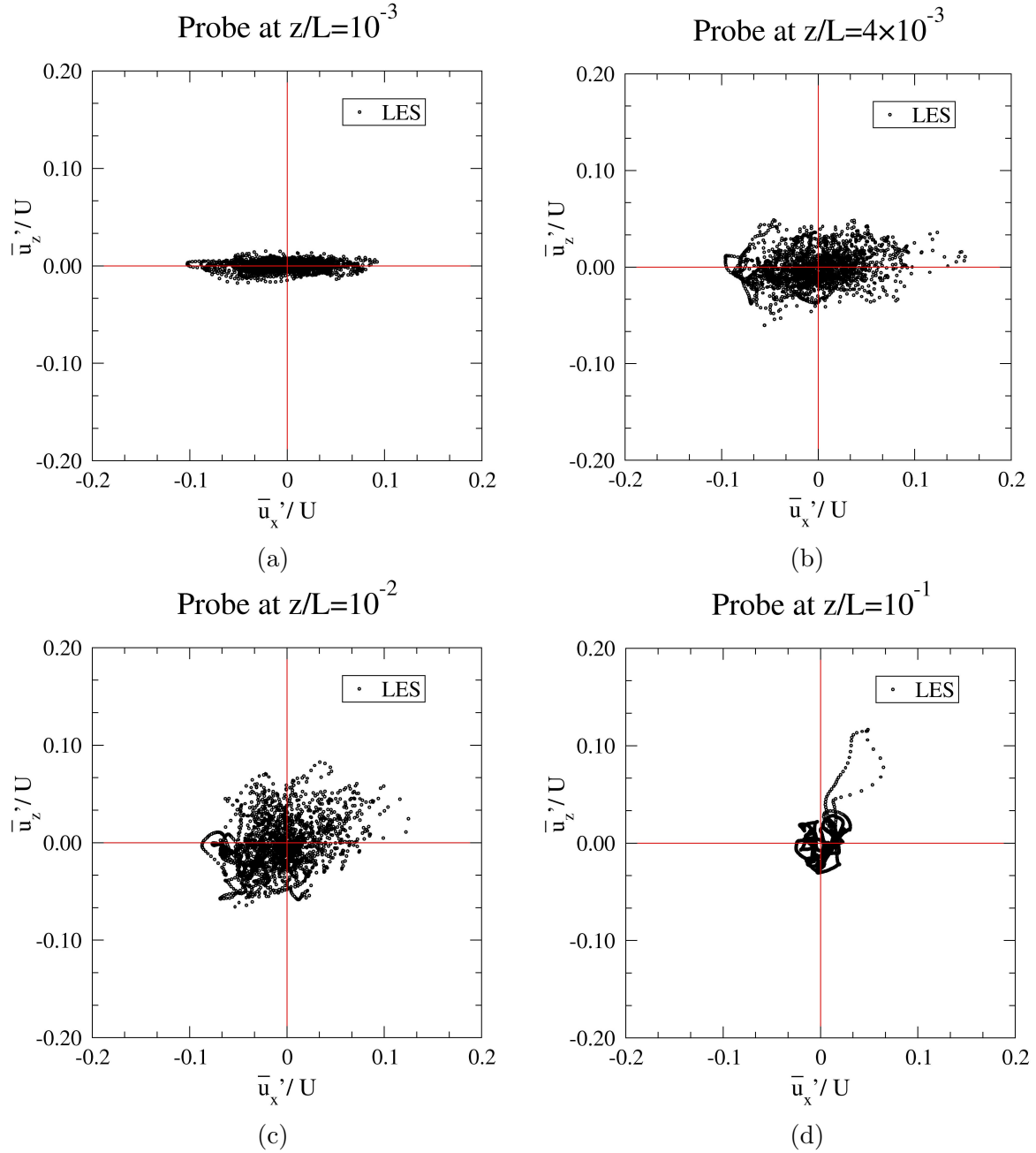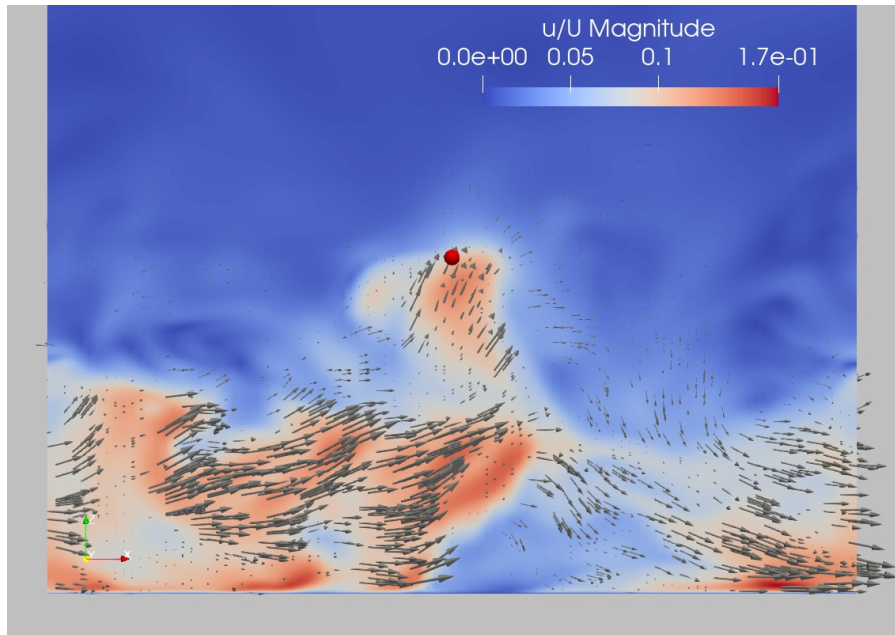
Figure 2.9: Scatter plots showing $\bar{u}'_z/U$ vs $\bar{u}'_x/U$ at the probe points located on the vertical of the domain centre: (a) $z/L = 10^{-3}$, (b) $z/L = 4 \times 10^{-3}$, (c) $z/L = 10^{-2}$ and (d) $z/L = 10^{-1}$.

(a) Vertical section passing through the domain centre and showing the velocity magnitude (colour plot) and the velocity projection on that plane (arrow plot) at time $t/T = 43.23$. The probe position is marked with a red dot. Only the lower part of the domain is visualized.
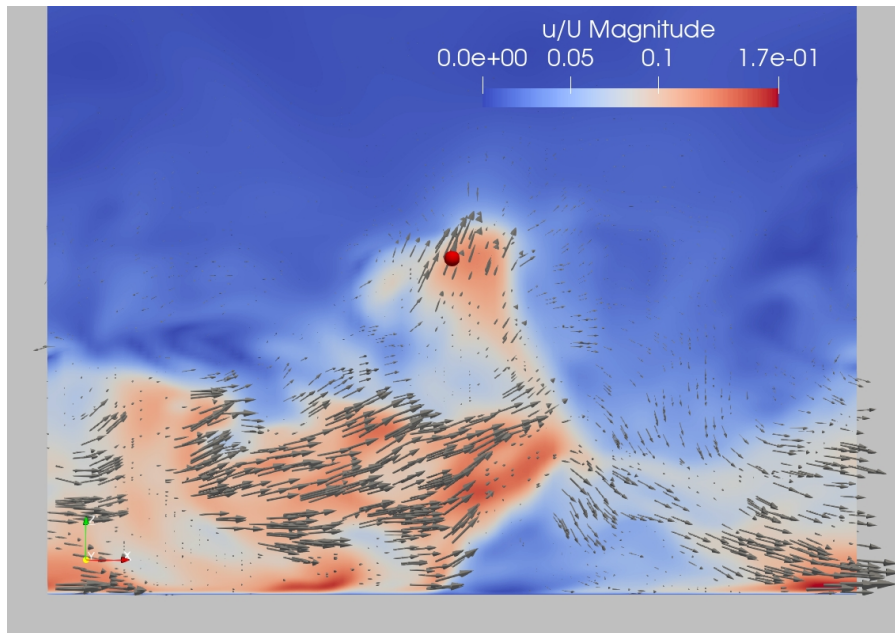
(b) Vertical section passing through the domain centre and showing the velocity magnitude (colour plot) and the velocity projection on that plane (arrow plot) at time $t/T = 43.44$. The probe position is marked with a red dot. Only the lower part of the domain is visualized.
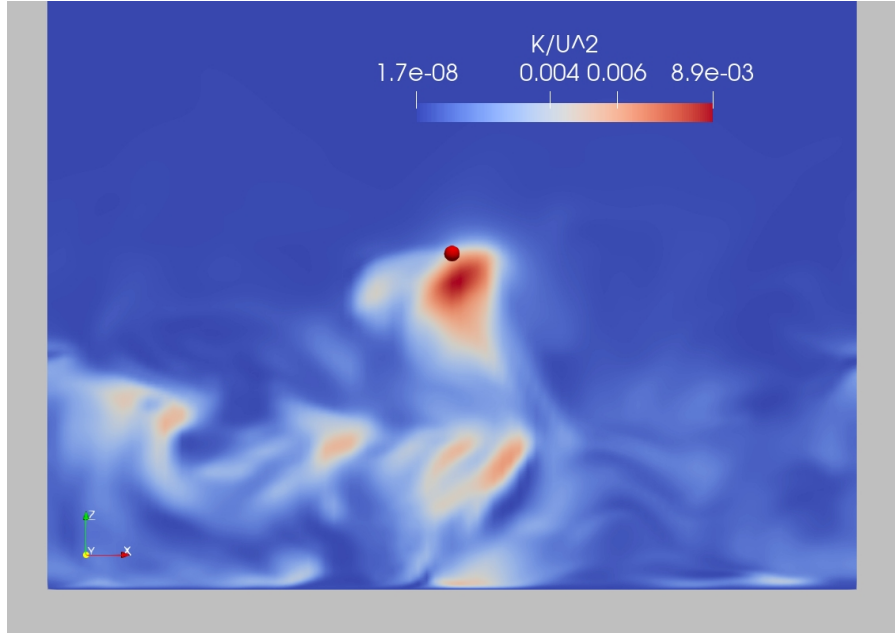
(a) Vertical section passing through the domain centre and showing TKE (colour plot) at time $t/T = 43.23$. The probe position is marked with a red dot. Only the lower part of the domain is visualized.

discrepancies have been noticed, which require further investigation. In general, it has been possible to distinguish three main zone in the vertical profile. A near-wall region (below $z/L \approx 3 \cdot 10^{-3}$) is characterized by an exponential decrease in the mean buoyancy and a corresponding increase in the mean stream-wise velocity. This layer shows a strong anisotropy, as demonstrated by both the velocity RMS vertical profiles and the scatter plot, and it is responsible for the flow development. Also, a thin zone is found in which the shear production is negative, thus showing an energy transfer from the turbulent to the mean flow. The intermediate region (from $z/L \approx 3 \cdot 10^{-3}$ to $z/L \approx 6 \cdot 10^{-2}$) exhibits fully developed mean stream-wise velocity and a slower decrease in the mean buoyancy, with intense upward buoyancy and momentum fluxes. In this region, both the velocity RMSs and the TKE reach the maximum value, being the buoyant production terms the main contributes in TKE budget. The anisotropy, conversely, progressively reduces at increasing distances from the floor. Far from the wall, in the outer layer (at z/L greater than $z/L \approx 6 \cdot 10^{-2}$), the flow intensity decreases, showing a narrow back-flow region and a negative-valued buoyancy layer. All the RMSs and the TKE decrease, while the buoyancy flux is characterized by a negative-value zone. Even though the flow is weaker, occasional upward flow structures may form, as verified in Fig.2.10a. In addition, the instantaneous fields have been displayed, showing the vertical plumes characterizing this type of flow. Finally, a test has been proposed to assess the simulation settings, verifying
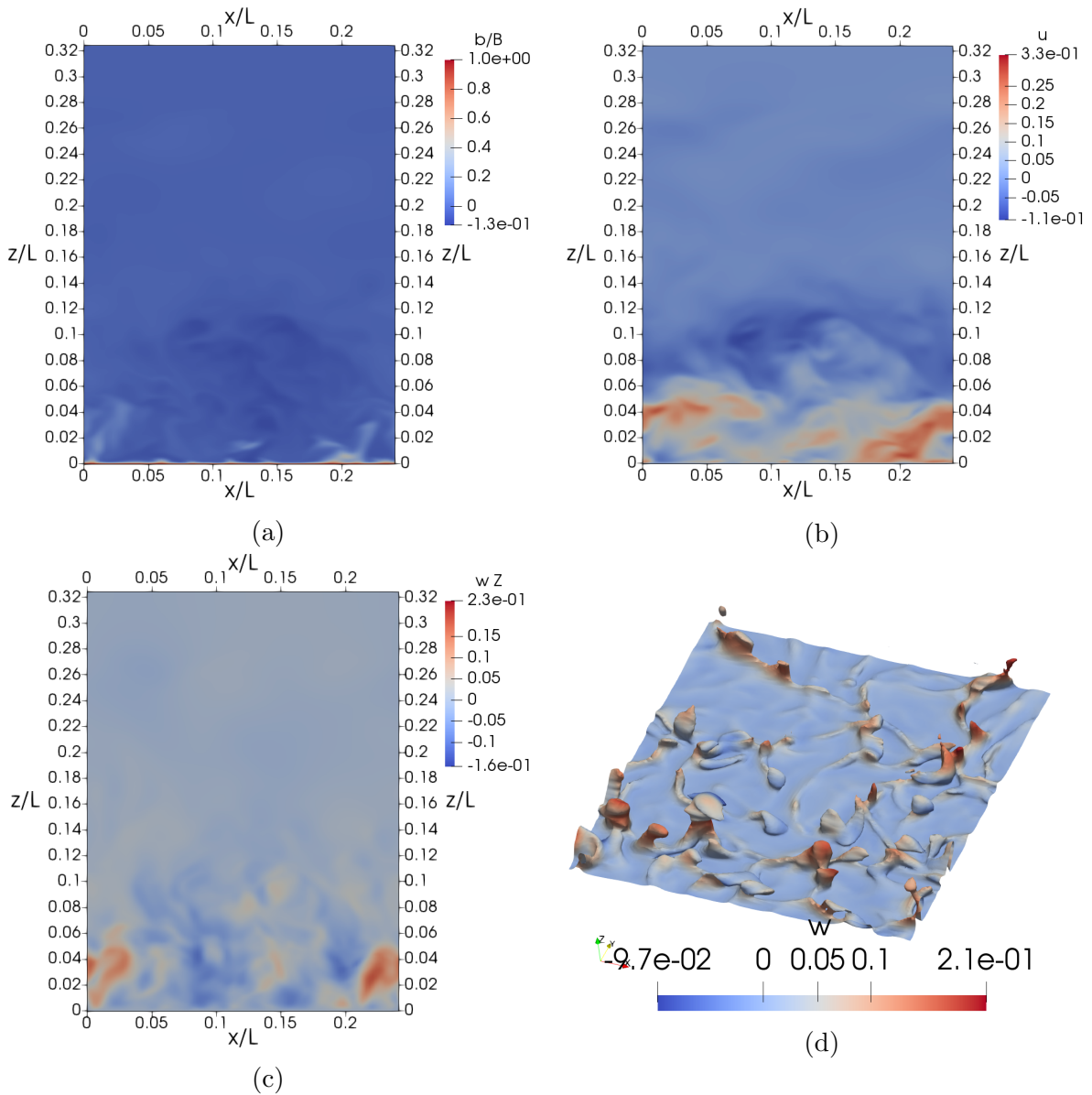
Figure 2.12: (a) Vertical section of the buoyancy at a fixed time; (b) vertical section of the x velocity component at a fixed time; (c) vertical section of the z velocity component at a fixed time; (d) 3D clipping, showing the upward flows organized in plumes. The surface is at a constant buoyancy value (conveniently chosen to show the flow structures), while the colour plot displays the vertical velocity component.
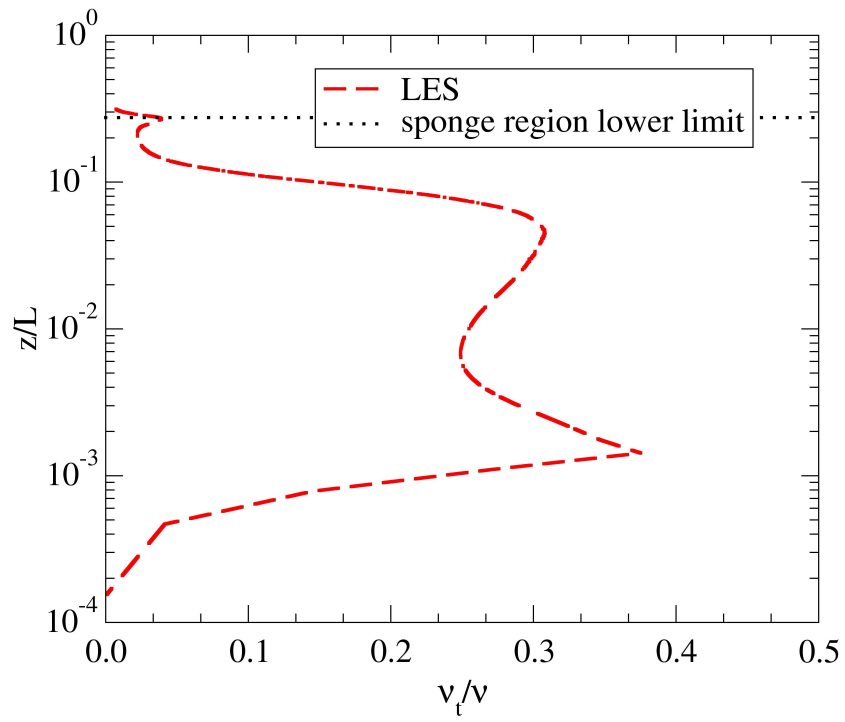
Figure 2.13: Vertical profile of the ν_t/ν ratio as a function of the normalized height.

that the mesh is appropriate to perform a LES-NWR.

Conclusion

Anabatic flows are of increasing importance in the atmospheric sciences. Their impact on the local circulations is known, but still under study. Phenomena like the air transport of pollutants are considerably affected by these currents in areas with complex terrains. Given the importance of the boundary layer in the flow development and the numerical cost of its resolution, the contribution offered by the Large-Eddy Simulation (LES) approach is valuable in this context.

For the present thesis, an anabatic flow has been successfully simulated through a LES with Near-Wall Resolution in OpenFOAM using a rectangular domain with a fixed inclination of 30°. A fixed homogenous buoyancy value has been imposed on the floor surface and a background stratification has been assumed. The Grashof number has been set to 2.1×10^{11}, the Prandtl number to 1.

Given the specific geometrical and physical features of the simulated case, the original OpenFOAM solver has required modifications. The modified solver accounts for a background stratification and it allows for cyclic boundary conditions on the vertical faces. Since the results of the simulation have shown an overall good agreement when compared with the DNS in [MG17], the case has been successfully validated. The advantages of the LES approach over the DNS is that the solution has been reproduced at a satisfactory level with a considerably smaller grid.

From the analysis of the results, three main layers can be recognized. First, a near-wall layer (below $z/L \approx 3 \cdot 10^{-3}$) is characterized by the development of the flow, showing an increase in the mean stream-wise velocity and an exponential decrease in the buoyancy. In this region, the anisotropy of the turbulence is maximum. Second, an intermediate layer (from $z/L \approx 3 \cdot 10^{-3}$ to $z/L \approx 6 \cdot 10^{-2}$) exhibits a fully developed flow, with a maximum in the mean stream-wise velocity and in the TKE. Third, an outer region (above $z/L \approx 6 \cdot 10^{-2}$) is characterized by a significant decrease in the kinematic quantities. In particular, it can be pointed out the presence of a weak back-flow region and a negative-valued buoyancy layer. In the outer layer, the anisotropy is minimum and occasional plumes may be seen.

The impact of turbulence has been discussed by comparing the mean velocity and buoyancy profiles with the laminar solution proposed by Prandtl [Pra42]. Overall, the presence of turbulence determines lower values in the maximum stream-wise velocity

and it widens the near-wall and the intermediate layers, being characterized by intense upward momentum and buoyancy fluxes.

Some discrepancies have been noticed, especially in the dissipation of turbulent kinetic energy, which require further investigations. In addition, future development may include the simulation of cases with higher Grashof numbers, so as to take full advantage of the LES's economy when compared to DNSs.

Acknowledgments

Bibliography

[BH18]   M. Harasek B. Haddadi, C. Jordan. *Tutorial Seven, Turbulence - Transient.* cfd.at, TU Wien, Wien, Austria, 2018.

[CR05]   et al. C. Reuten. Observations of the relation between upslope flows and the convective boundary layer in steep terrain. *Boundary-Layer Meteorology*, 116:37–61, 2005.

[EF09]   A. Shapiro E. Fedorovich. Structure of numerically simulated katabatic and anabatic flows along steep slopes. *Acta Geophysica*, 57(4):981–1010, 2009.

[FM16]   M. Darwish F. Moukalled, L. Mangani. *The Finite Volume Method in Computational Fluid Dynamics.* Springer, Switzerland, 2016.

[Gre15]   C.J. Greenshields. *Programmer's Guide.* OpenFOAM Foundation Ltd, England, 2015.

[Jas09]   H. Jasak. Dynamic mesh handling in openfoam. 01 2009.

[Lil66]   D.K. Lilly. *The representation of small-scale turbulence in numerical simulation experiments.* NCAR, Colorado, USA, 1966.

[McN82]   R.T. McNider. A note on velocity fluctuations in drainage flows. *J. Atmospheric Sciences*, 1(116):1658–1660, 1982.

[MG17]   et al. M.G. Giometto. Direct numerical simulation of turbulent slope flows up to grashof number gr=2.1e11. *J. Fluid Mechanics*, 829:589–620, 2017.

[Ope]   OpenFOAM. Openfoam: User guide v2006.

[PK04]   I.M. Cohen P.K. Kundu. *Fluid Mechanics.* Elsevier Academic Press, San Diego, California, USA, 2004.

[PM82]   J. Kim P. Moin. Numerical investigation of turbulent channel flow. *J. Fluid Mechanics*, 118:341–377, 1982.

[PO01]   R.I. Issa P.J. Oliveira. An improved piso algorithm for the computation of buoyancy-drivenflows. *Numerical Heat Transfer*, 40(B):473–493, 2001.

[Pop00] S.B. Pope. *Turbulent Flows*. Cambridge University Press, Cambridge, UK, 2000.

[Pra42] L. Prandtl. Stromungslehre. *Vieweg, Braunschweig*, pages 396–399, 1942.

[Ric22] L.F. Richardson. *Weather Prediction by Numerical Process*. Cambridge University Press, Cambridge, UK, 1922.

[Sch90] U. Schumann. Large-eddy simulation of the up-slope boundary layer. *Q. J. R. Meteorol. Soc.*, 1(116):637–670, 1990.

[Sma63] C. Smagorinsky. General circulation experiments with the primitive equations. *Monthly Weather Review*, 91(3):99–164, 1963.

[TK89]   J. Kondo T. Kuwagata. Observation and modeling of thermally induced upslope flow. *Boundary-Layer Meteorology*, 49:265–293, 1989.